NEUROSCIENCE

A distinct lineage pathway drives parvalbumin chandelier cell fate in human interneuron reprogramming

Christina A. Stamouli[1], Alexander Degener[2], Efrain Cepeda-Prado[1], Andreas Bruzelius[1], Emil Andersson[2], Jessica Giacomoni[3], Aurélie Delphine Vorgeat[1], Srisaiyini Kidnapillai[1], Oxana Klementieva[4], Malin Parmar[3], Victor Olariu[2], Daniella Rylander Ottosson[1]*

Direct lineage reprogramming of glial cells to induced neurons has the potential for restoring brain circuits and function in neuronal disorders and states. We introduce three-dimensional (3D) human glia reprogramming into neurons with a GABAergic interneuron phenotype using stem cell–derived human glia. Single-nucleus RNA sequencing of the converted cells demonstrates distinct neuronal clusters within 2 weeks, including a parvalbumin (PV) cluster with high neuronal maturity and features of chandelier interneurons. A lineage trajectory analysis of the glia-to-neuron conversion reveals a distinct lineage pathway to PV chandelier fate, including various neuronal developmental stages and the establishment of synaptic machinery. This analysis reveals PV fate-important genes that are previously unknown to neural reprogramming with promising functional importance for future derivations. Our data demonstrate successful human glia conversion into interneurons with features of bona fide PV subtype and highlight the reprogramming trajectory with key transitional genes. This advancement holds promise for future human brain cell engineering and repair.

INTRODUCTION

Neural reprogramming offers a promising approach to brain repair strategies and is a growing field of research (*1*). With this technique, non-neuronal cells can be converted into neurons using specific combinations of key transcription factors, miRNAs, and/or small-molecule cocktails (*2*). This approach bypasses the pluripotency step, making it feasible for in-brain repair with a low risk of tumorigenesis (*3*). We and others have shown that resident mouse glial cells can be directly reprogrammed into neurons (*4*–*10*), including parvalbumin (PV) interneurons (*11*–*13*). Glial progenitor cells (GPCs) are particularly suitable for therapeutic in vivo reprogramming due to their proliferative nature in adulthood and widespread distribution throughout the brain parenchyma (*14*–*16*). However, transferring glia reprogramming to the human system can be challenging due to the late embryonic development of human GPCs (hGPCs) (*17*). We have adressed this using a stem cell differentiation protocol of hGPCs (*18*, *19*) that yields primarily oligodendrocyte precursor cells (OPCs), and shown successful conversion of these cells into interneurons (*20*).

In the cerebral cortex, excitatory principal glutamatergic neurons and inhibitory GABAergic interneurons are the two main neuronal types responsible for excitation and inhibition (*21*). Among these, the PV-expressing interneurons have unique morphological and functional properties that render them crucial in neural circuits and memory processing (*22*). Recent evidence links PV interneuron loss or dysfunction to several neurological and neuropsychiatric diseases (*23*–*27*), a change that is critical in the underlying neuronal network dysfunction and cognitive decline. These data underscore the need for improved strategies for generating and replacing PV interneurons in the diseased brain. Experimental studies indicate that restoration of GABAergic interneurons via cell transplantation could counteract disease pathology, such as that seen in epilepsy (*25*, *27*–*29*). However, generating subtype-specific PV interneurons in vitro from stem cells or fetal sources has proven difficult (*29*–*33*).

Herein, we introduce three-dimensional (3D) human glia reprogramming to interneurons, including the PV subtype, as a novel strategy for interneuron repair. Human stem cell–derived GPCs were transduced (*20*, *34*), and successfully converted into inhibitory neurons with functional properties within weeks, in contrast to stem cell–derived protocols that typically take months. Single-cell transcriptomics revealed a characteristic pallial interneuron phenotype, including a distinct PV-enriched cluster with features of primary human chandelier interneurons. Lineage trajectory analysis of the glia reprogramming demonstrated a distinct PV pathway involving several dynamic genes that have not been seen before for human neural reprogramming. In vitro manipulation of these holds functional potential for future PV derivation, both for directed stem cell differentiation and through direct reprogramming.

In conclusion, we present human glia reprogramming to neurons with a transcriptional and protein signature of PV interneurons along with the underlying trajectory pathway. This holds potential for patient-specific within-brain repair for neurological disorders linked to interneuron dysfunction using human glia reprogramming.

RESULTS

Neuronal reprogramming of human glia precursor cells

Human stem cell–derived GPCs were derived from embryonic stem cells (hESCs) according to previous established protocols (*18*, *19*).

[1]Group of Regenerative Neurophysiology, Wallenberg Neuroscience Center, Lund Stem Cell Center and MultiPark strategic neuroscience network, Department of Experimental Medical Science, Faculty of Medicine, Lund University, Lund, Sweden. [2]Group of Computational Science for Health and Environment, Center for Environmental and Climate Science, Lund University, Lund, Sweden. [3]Group of Developmental and Regenerative Neurobiology, Wallenberg Neuroscience Center and Lund Stem Cell Center, Department of Experimental Medical Science, Faculty of Medicine, Lund University, Lund, Sweden. [4]Group of Medical Spectroscopy, Department of Experimental Medical Science, Faculty of Medicine, Lund University, Lund, Sweden.
*Corresponding author. Email: daniella.ottosson@med.lu.se

hGPCs exhibited typical bipolar morphology (Fig. 1B) and expressed Platelet Derived Growth Factor Alpha (PDGFRα) and Glial Fibrillary Acidic protein (GFAP), labeling OPCs and astrocyte biased precursors, respectively [Fig. 1C, 36.2% PDGFRA+ cells, 23.1% GFAP+ cells, and 10.8% double-positive cells, with remaining proportion unknown (*19*)]. They expressed OPC marker SRY-Box Transcription Factor 10 (SOX10) (75% of total cells; fig. S1, B and C) (*35*) but low levels of neuronal stem cell markers Nestin and Sox2 and immature neuronal marker Doublecortin (DCX) (fig. S1B). hGPCs were also positive for Gamma-Aminobutyric Acid (GABA) as previously shown [fig. S1, A and C, 69% of GABA+/4′,6-diamidino-2-phenylindole (DAPI) cells, where 53% coexpressed PDGFRA and 7.5% coexpressed GFAP (*36*)].

hGPCs were seeded in ultralow attachment plates along with lentiviral vectors carrying five reprogramming factors (*Ascl1*, *DLX5*, *LHX6*, *Sox2*, and *FOXG1*; ADLSF) in a dual regulation system, i.e., ADL was on constitutive expression and S and F on Dox regulation (*20*) (Fig. 1A). Cells rapidly self-aggregated into 3D spheroids and were cultured for up to 50 days (Fig. 1D). For control groups, hGPCs were kept for 21 days without ADLSF combination in both glial medium (GM) and neuronal differentiation medium (ND). An initial immunocytochemistry assessment demonstrated clear induction of the neuronal marker TAU (tubulin-associated protein) in the ADLSF group (Fig. 1E) along with a complete decline of PDGFRα and GFAP and the absence of proliferative markers (fig. S1E). In this group, we could detect some DCX+ cells with low expression of NEUN+ nuclei (fig. S1D). In the control groups on the other hand, neuronal TAU and NEUN proteins were absent (Fig. 1E and fig. S1D), and few DCX+ cells were detected (fig. S1D). These control groups instead remained positive for PDGFRα and GFAP and showed continued proliferation (Fig. 1, E and F).

In line with this, reverse transcription quantitative polymerase chain reaction (RT-qPCR) demonstrated up-regulation of pan-neuronal genes Synaptophysin 1 (*SYP1*) and Synapsin 1 (*SYN1*) in the ADLSF group (Fig. 1G). Here, we could further confirm the presence of all of the individual transgenes at days 7, 13, and 21 (fig. S1E), highlighting the contribution of the viral cocktail to the neuronal conversion. These results indicate a neuronal switch in the ADLSF group and remaining glial identity in the controls.

To confirm a switch in glia cell identity, we exclusively applied optical photothermal infrared (O-PTIR) microspectroscopy on cryosections of ADLSF-reprogrammed and control spheroids (Fig. 1H). We used label-free biospectroscopic analysis to examine cellular heterogeneity and molecular changes across different regions of the spheroid, focusing on comparisons between cells at the edge and the center. Although spectroscopy does not allow for precise identification of specific cell types, it is a powerful tool for detecting biochemical changes, such as shifts in protein structure, lipid composition, and metabolite content, associated with cellular transformation.

Spectra from both outer and inner zones showed similar spectra position and intensity, indicating cellular homogeneity throughout the spheroid and good cell viability also in the core (Fig. 1H). We could detect a change in intracellular biomolecules such as metabolites, lipids, and proteins upon ADLSF transduction in their spectral intensities, indicating cellular response to the treatment (Fig. 1, I to K with the red cluster distinct from the blue and black cluster). This suggests a consistent and widespread induction to a new cell type that is distinct from the original GPC, with changes evident throughout the spheroid.

Together, these data demonstrate successful neuronal conversion in a 3D culture system that is transcription factor–dependent and that involves changes in cellular biomolecular composition.

Human glia-to-neural reprogramming shows early fate dynamics

To unravel the transcriptional dynamics underlying the glia-to-neuron transition, we performed a 10x Genomics droplet-based single-nuclei RNA sequencing (snRNA-seq) of ADLSF reprogrammed glia at day 0, 1, 3, 7, 13, and 21 and in controls (GM and ND) at day 21 (*37*). In total, 21,276 single nuclei were profiled after quality filtering (table S2, one biological replicate). At day 0, the cells expressed classical astrocytic markers *GFAP* and SRY-Box Transcription Factor 9 (*SOX9*) (*38*) and the classical OPC markers *PDGFRA* and *SOX6* (*35*, *38*) (Fig. 2C and fig. S2). A subset of cells expressed the pre-OPC markers Protein Tyrosine Phosphatase Receptor Type Z1 (*PTPRZ1*), *EGFR*, and *F3* (*35*, *38*, *39*), but few cells showed NSC marker *NES* and *SOX2* (fig. S2A, *PDGFRA* coexpression of *NES*: 8.24% and *SOX2*: 15.19%) and doublecortin (*DCX*) (fig. S2E). The transcript at day 0 was successfully integrated with human primary cortical OPCs (*40*) (fig. S2B with cells in cluster 8 showing a cosine similarity score of 0.57), supporting an OPC phenotype.

From this state onward, distinct transcriptional clusters appeared throughout the process (Fig. 2, A and B), as early as days 3 to 7, and followed by a full transcriptomic switch at days 7 to 13. By day 21, a new cluster emerged that was transcriptionally more similar to the earlier time points (likely due to increased fragility of mature neurons, which may have been lost during nuclei extraction, thus a bias toward immature cells; see table S2 for cell counts). The neuronal reprogramming process did not involve much apoptosis as low levels were detected for Caspase 3 (*CASP3*), BCL2 Associated X (*BAX*), and Fas Cell Surface Death Receptor (*FAS*) (fig. S2C). Very few cells expressed the cycling gene *TOP2A* (fig. S2C).

To corroborate these findings, we repeated the reprogramming procedure and performed snRNA-seq on a new biological replicate at day 7 and integrated this sample with original dataset from day 1 to 21 to assess cell type distribution. Figure S2D shows the cosine similarity to the day 7 replicate and the position in our original Uniform Manifold Approximation and Projection (UMAP) (Fig. 2B), demonstrating a clear overlap. This suggests a consistent reprogramming outcome for our protocol and robust neuronal induction.

The reprogramming process further followed a glia-to-neuron transition as demonstrated with glial marker-, immature and mature neuronal genes expressed at different stages of the process (Fig. 2C). *GFAP* and *PDGFRA* were gradually down-regulated during the process, whereas the immature neuronal genes Tubulin Beta 3 Class III (*TUBB3*) and *TUBB2B* were transiently expressed at day 3 and declined by day 7 (Fig. 2C). Although hGPCs expressed *DCX* at day 0 [fig. S2E as previously shown (*41*)], its expression further increased at the earlier stages of reprogramming (fig. S2 for *DCX* expression at all time points). The mature neuronal genes *SYN2* and *SYN3* were mainly detected in the clusters appearing on days 7 to 13 [Fig. 2C, 38.9% *SYN3*+ cells at day 13 as in (*20*)]. Day 21 cluster did not show these markers and was instead similar to ND controls but yet different from GM, suggesting an immature neuronal state. There was concurrent expression of endogenous transcription factors (*DLX5*, *SOX2*, and *FOXG1*) mirroring the viral transduction, most likely due to a reinforcing action of transgenes (fig. S2F).

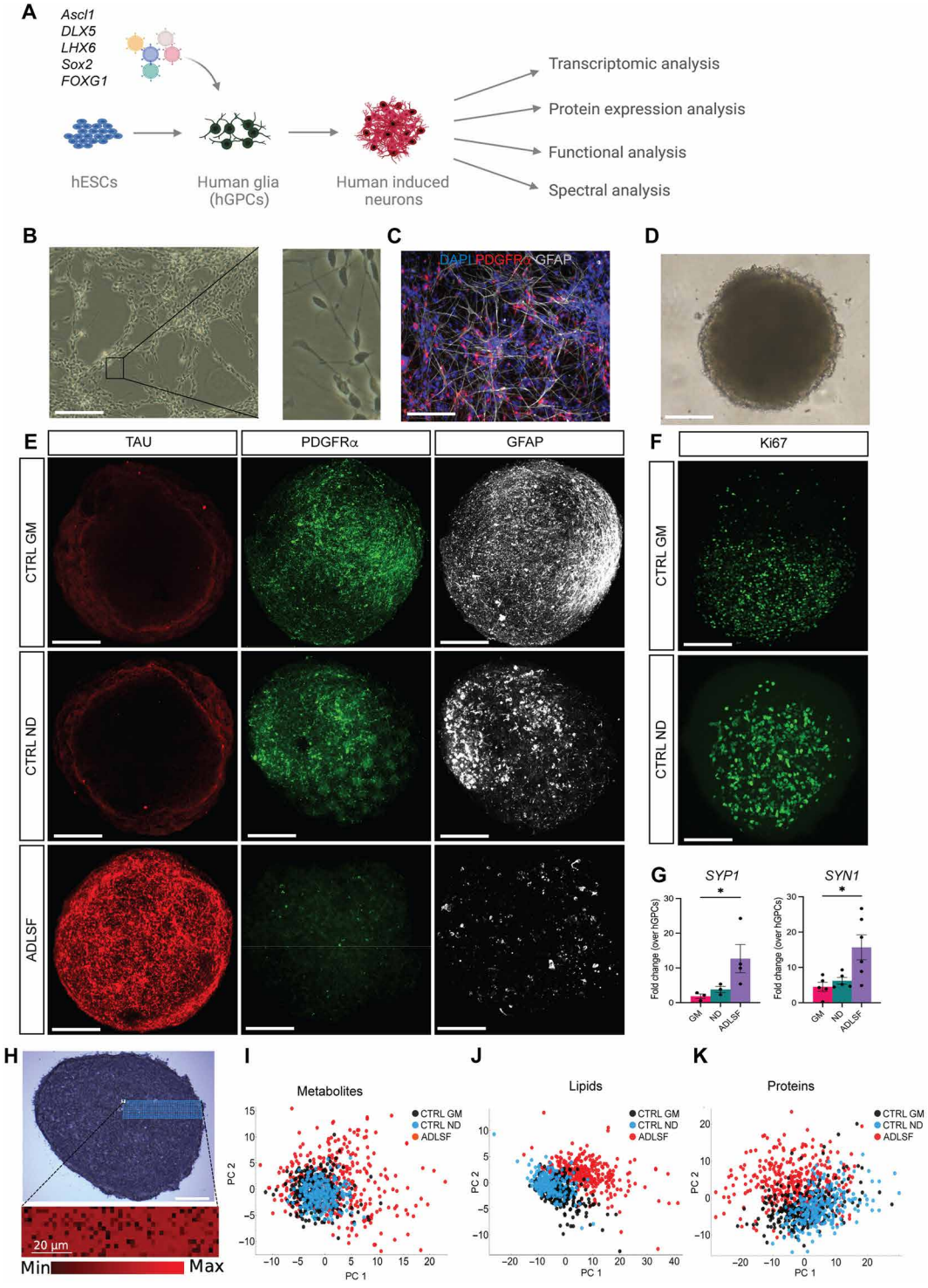

Fig. 1. Neuronal reprogramming of human glia precursor cells. (**A**) Schematic overview of the experimental design. (**B**) Bright-field photo of hGPCs in 2D culture at day 280 of differentiation. (**C**) Immunocytochemistry of hGPCs demonstrates the presence of glial markers PDGFRα and GFAP (see also fig. S1, A to C). (**D**) Bright-field photo of induced 3D spheroid. (**E**) Maximum intensity projections of immunostainings for TAU, PDGFRα, and GFAP at day 21 for ADLSF-transduced cells, and glial cells in GM and ND (see also fig. S1D). (**F**) Maximum intensity projections of immunostaining for proliferation marker MKi67 in GM and ND controls at day 21 (see also fig. S1E). (**G**) RT-qPCR analysis of *SYN1* and *SYP1* at day 21 ($n = 3$ to 5 for GM and ND, $n = 3$ to 6 for ADLSF, n = biological replicate): $^*P < 0.05$. One-way ANOVA test and post hoc Tukey test were performed for *SYN1*, and Kruskal-Wallis with uncorrected Dunn's test was performed for *SYP1*. (**H**) A bright-field overview of induced neuron spheroid. Blue dots indicate spectral positions and intensity distribution at 1656 cm^{-1}. Black spectra corresponding to low intensity were removed. (**I** to **K**) PCA of (I) metabolites, (J) lipids, and (K) proteins in the ADLSF condition compared with ND and GM controls at day 21. Scale bars, 100 µm. Data are presented as means ± SEM.

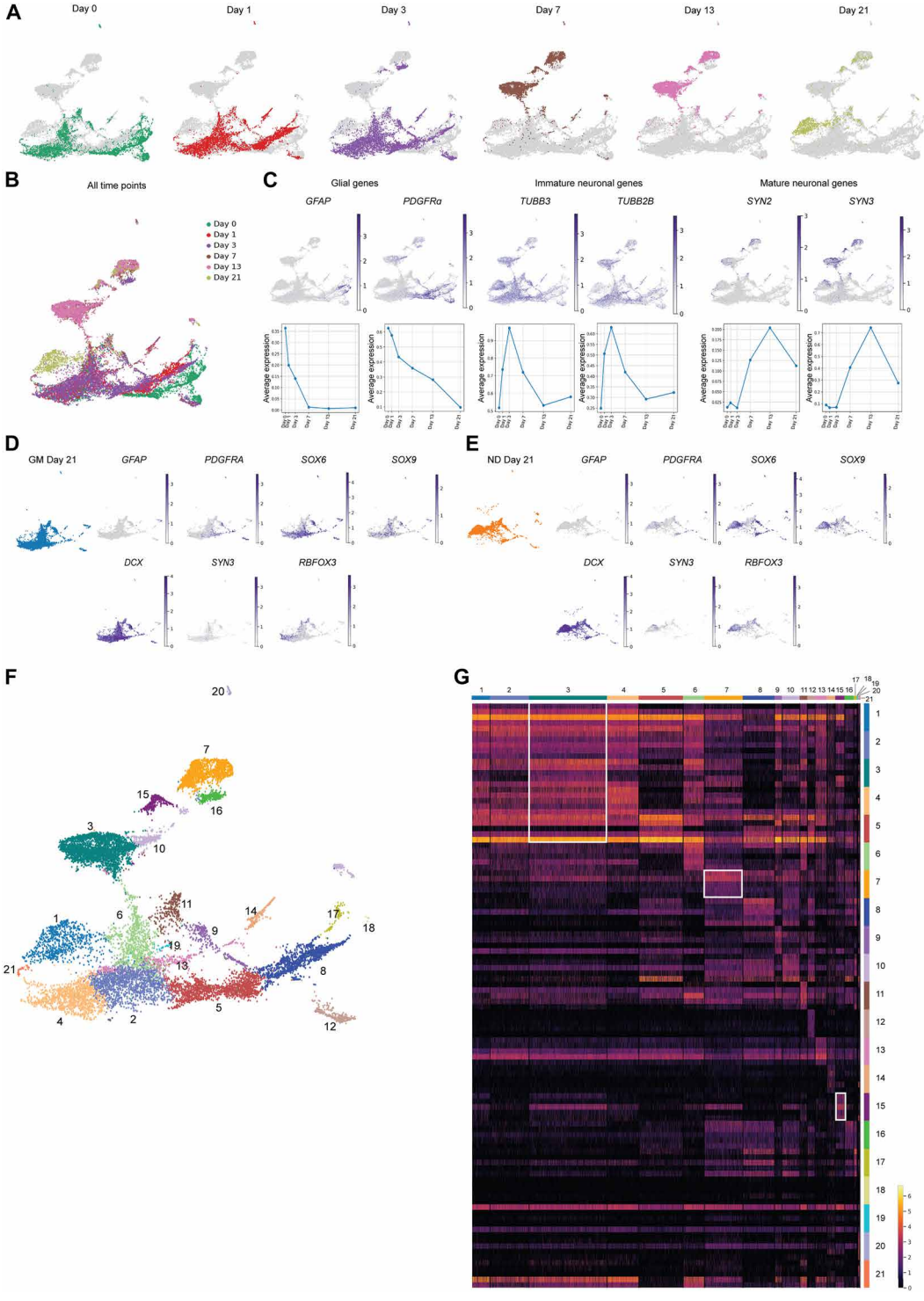

Fig. 2. Human glia-to-neural reprogramming shows early fate dynamics. (**A**) UMAP plots at different time points (day 0, 1, 3, 7, 13, and 21) during the reprogramming process (see also fig. S2, A and B). (**B**) UMAP plot with all time points combined. (**C**) UMAP plots of glial- (*GFAP* and *PDGFRA*), immature neuronal (*TUBB3* and *TUBB2B*), and mature neuronal genes (*SYN2* and *SYN3*) with average expression levels over time (see also fig. S2C). (**D** and **E**) UMAP plots of glial genes *GFAP*, *PDGFRA*, *SOX6*, *SOX9*, *DCX*, *SYN3*, and *RBFOX3* for (D) GM control at day 21 and (E) ND control at day 21 (see also fig. S3). (**F**) UMAP plot based on Leiden clustering. (**G**) Heatmap showing differentially expressed genes in clusters generated by Leiden.

In contrast to the experimental condition, the control groups (at day 21) maintained their glial fate throughout the process, with classical glial marker expression, e.g., *GFAP* (3% in GM, 1.4% in ND), *PDGFRA* (9.9% in GM, 6% in ND), *SOX6* (46.9% in GM, 38.6% in ND), and *SOX9* (11.1% in GM, 13.2% in ND) (Fig. 2, D and E, and fig. S3A). A slightly different cell population was seen in the ND control, compared to the GM control, possibly reflecting transcriptional changes resulting from the long-term ND medium with small molecules and growth factors. Nevertheless, both controls expressed glial markers in similar proportions and *DCX* immature neuronal marker and were negative for neuronal markers, e.g., TAU protein, *SYN3*, and *RBFOX3* (Figs. 1E and 2, D and E, respectively, 1.7% *SYN3*+ for GM, 3.1% for ND), demonstrating no neuronal conversion in controls. Together, this validates a distinct glia-to-neuron transcriptional process that depends on ADLSF transduction.

To further support the transcriptional reprogramming changes, the transcriptome clusters were analyzed in an unbiased approach for all time points using Leiden clustering. Clustering with a resolution of 0.95 produced 22 distinct gene clusters (Fig. 2F). Differential gene expression analysis on these clusters using the Wilcoxon rank sum test [top five differentially expressed genes (DEGs) per cluster] is visualized in Fig. 2G as a heatmap and demonstrated transcriptional differences. Clusters 7 and 15, defined as neuronal clusters (Fig. 2C), showed a distinct transcriptional signature (Fig. 2G) with neuronal markers (53 and 78% MAPT expression, respectively). Although cluster 3 expressed mature neuronal markers (Fig. 2C, 73% MAPT), it seemed to be transcriptionally close to clusters 1, 2, 4, and 5 (Fig. 2G) representing earlier time points implying an immature neuronal or "confused" cluster. Although we did not see transcriptionally distinct subclusters for cluster 3, both clusters 7 and 16 appeared naturally as subclusters at higher resolutions. These results support a transcriptional dynamic process with distinct clusters at different neuronal maturation stages, where specifically clusters 3, 7, and 15 separate from earlier time points and from each other (see DEGs for these clusters in table S5).

Neural reprogramming shows gradual functional maturity

To assess the function of the reprogrammed neuronal fate, we performed pathway analysis and specifically a Gene Set Enrichment Analysis (GSEA) study. Here we could confirm the acquisition of a neuronal fate, switching from immature pathways, e.g., Neuroepithelial cell differentiation pathway, into more neuronal-specific pathways from day 7, e.g., Neurotransmitter-Gated Ion Channel, Voltage-Gated Sodium Channel activity, and Excitatory Postsynaptic Potential regulation (Fig. 3A). The Neuroepithelial cell differentiation pathway reappeared at day 21, further supporting the neuronal loss at this time point. Next, we sought to investigate the differentially expressed genes involved in ADLSF-induced pathways and could further confirm a glial fate at earlier time points (days 0 to 3), with expressions of *CD44*, *GFAP*, *PDGFRA*, and *PTPRZ1* (Fig. 3B). From day 7 to 21, genes involved in pivotal neuronal processes appeared, e.g., synaptic membrane compartment (Neuroligin 1: *NLGN1*) (Fig. 3B). Also presynaptic active zone genes, such as Regulating Synaptic Membrane Exocytosis 2 (*RIMS2*) and synaptic membrane genes ELKS/RAB6-Interacting/CAST Family Member 2 (*ERC2*) were strongly induced from day 7 along with a functional neuronal state and synapse formation. In line with this, genes related to Voltage-Gated Sodium Channel Activity, such as Fibroblast Growth Factor 14 (*FGF14*) and Fibroblast Growth Factor 12 (*FGF12*), were up-regulated from day 7, with highest expression at day 13, whereas genes involved in excitatory postsynaptic potential, e.g., AMPA or *N*-methyl-D-aspartate (NMDA) receptors (*GRIA1* and *GRIN2B*, encoding for the GluN2B subunit), were more highly expressed from day 7 to 21 (Fig. 3B), supporting synaptic compartment formation and functional neuronal membrane properties. Together, this GSEA pathway study demonstrates a transcriptomic switch from a glial precursor state to a functional neuronal state with synaptic compartment formation in only 13 days of reprogramming.

To further prove a functional neuronal state for the continuously maturing neurons in the 3D culture, we performed patch-clamp electrophysiology on free-floating spheroids at 7 to 50 days (Fig. 3, C to H, and table S6). This showed a gradual functional improvement of intrinsic membrane properties throughout the reprogramming process. The input resistance (*Ri*) was reduced on days 13 and 21, indicating an increased number of voltage-gated channels. Membrane capacitance (*Cm*) was increased from day 21 and suggested increased cell size (Fig. 3D). At all time points, rectifying inward sodium (Na^+) and outward potassium (K^+) were detected (Fig. 3E) with a gradual increase in Na^+ amplitude at days 21 and 50 (Fig. 3F). The resting membrane potential (RMP) was more hyperpolarized on day 50 compared to day 13. Whereas the action potential (AP) threshold was similar among time points, the AP amplitude and afterhyperpolarization (AHP) differed between day 50 and the earlier time points, suggesting an improved functional neuronal maturation (Fig. 3G). Similarly, the ability to fire repetitive series of evoked APs upon current injection was superior at day 50 compared to day 21 (Fig. 3H), as was the firing rate (Fig. 3I).

Spontaneous postsynaptic activity recorded at 21 days in vitro (DIV) was not affected by the presence of glutamatergic antagonist (5 μM NBQX and 50 μM D-APV) but was completely abolished by the $GABA_A$ receptor antagonist picrotoxin (100 μM PTX) (Fig. 3J), indicating functional GABAergic synaptic communication. Overall, these data indicate a gradual maturation of neuronal function in long-term 3D cultures that is in line with the protracted maturation process of neurons in vitro (*30*).

Rapid induction into pallidal GABAergic neurons with mature neuronal signaling

Following the sequencing analysis, we continued investigating the clusters on days 3 to 7, labeled by numbers and color: 3 (dark green), 15 (purple), 7 (yellow), and 16 (lime) (Fig. 4A). These clusters were all positive for GABAergic marker *GAD1* (Fig. 4B, 57% of the *SYN3*+ cells coexpressed GAD1 at day 13).

A scatterplot revealed that approximately two-thirds of *SYN3* cells from day 7 to 21 coexpressed *GAD1* ($n = 1274$ cells of a total of 1888 *SYN3*+ cells), indicating an inhibitory neuronal population. Fewer cells expressed glutamatergic marker, e.g., Solute Carrier Family 17 Member 7 (*SLC17A7*), *VGLUT-1*, Protein Phosphatase 1 Regulatory Inhibitor Subunit 1B (*PPP1R1B*), and medium spiny neuron marker *DARPP-32* (fig. S4A).

Further analysis demonstrated expression of Sodium Voltage-Gated Channel Alpha Subunit 1 Nav1.1 (*SCN1A*) (*42*) and, particularly in the purple cluster, Solute Carrier Family 6 Member 1 (*SLC6A1*) or *GAT-1*, a marker mainly expressed in chandelier interneurons (*43*, *44*) (Fig. 4D). All neuronal clusters expressed genes for different GABA receptor subunits that facilitate communication with inhibitory neurons, e.g., Gamma-Aminobutyric Acid Type A Receptor Subunit Alpha 2 (*GABRA2*) and Subunit Beta1 (*GABRB1*) (*45*) (Fig. 4D).

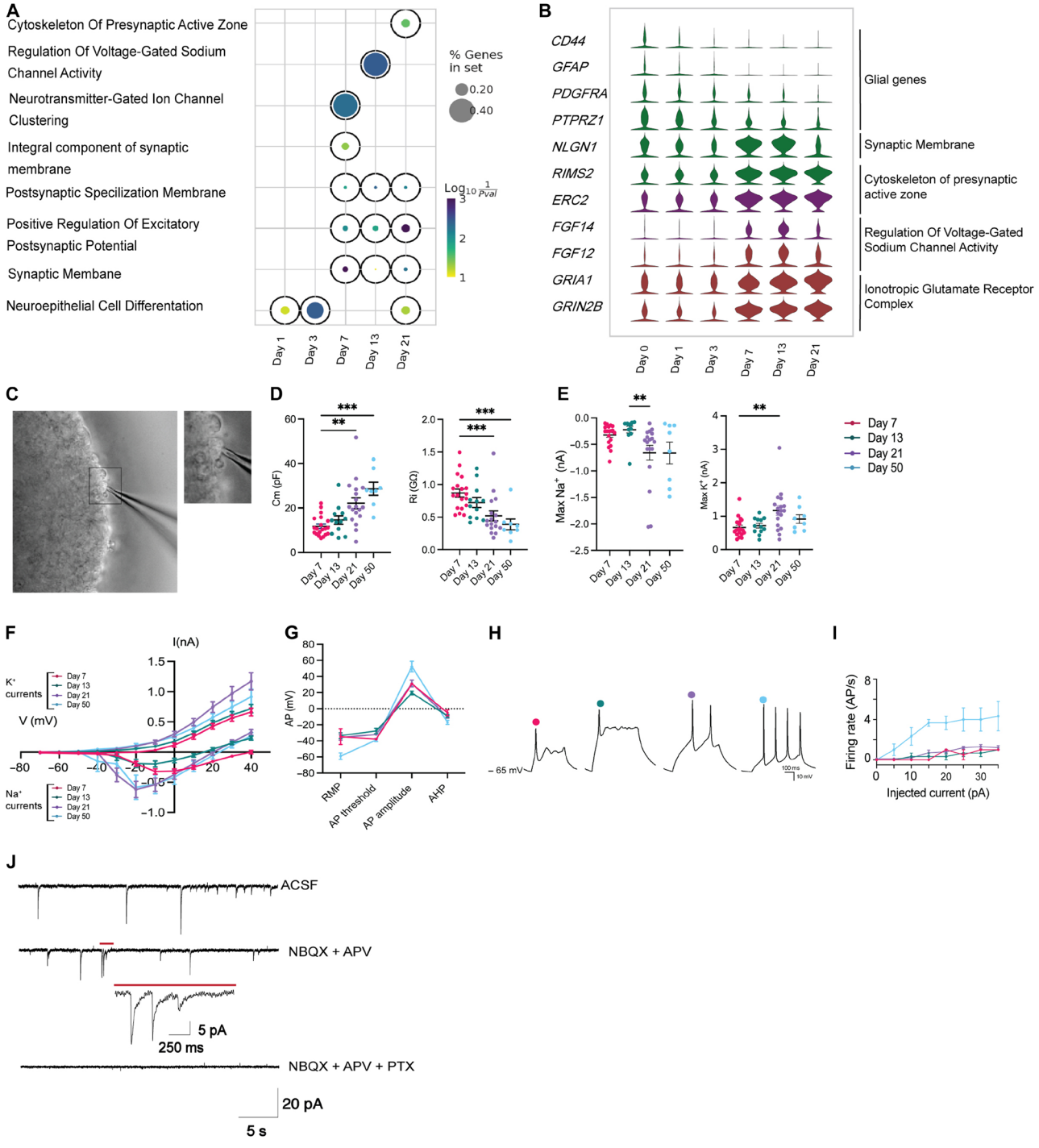

Fig. 3. Neuronal reprogramming shows gradual functional maturity. (**A**) Pathway analysis of day 1 to 21 of reprogramming. (**B**) Violin plot showing differentially expressed genes during the process. (**C**) Bright-field photo of patch-clamp electrophysiology of a free-floating induced neuron spheroid, day 21. (**D**) Passive membrane properties of reprogrammed neuron at different time points (n = 19 to 20 for day 7, n = 12 for day 13, n = 17 to 18 for day 21, n = 8 for day 50, n = individual cell): $^{**}P < 0.01$; $^{***}P < 0.005$, Kruskal-Wallis test with uncorrected Dunn's test. (**E**) Maximum sodium (Na^+) and maximum potassium (K^+) currents at different time points demonstrating an increase in current over time (n = 20 for day 7, n = 12 for day 13, n = 18 for day 21, n = 8 for day 50, n = individual cell): $^{**}P < 0.01$, Kruskal-Wallis test with uncorrected Dunn's test. (**F**) Inward Na^+ and outward K^+ currents plotted against stepwise voltage induction (right), maximum Na^+ current (middle), and maximum K^+ current (left) (n = 20 for day 7, n = 12 for day 13, n = 18 for day 21, n = 8 for day 50, n = individual cell). (**G**) AP properties, RMP, AP threshold, AP amplitude, and AHP (n = 2 for day 7, n = 3 for day 13, n = 11 for day 21, n = 3 for day 50, n = individual cell). (**H**) Representative traces of induced AP recorded at distinct time points, with colored dots indicating the time points. (**I**) AP frequency, with the number of AP/s (hertz) for the distinct time point and with increasing current injection. (**J**) Sample traces of postsynaptic activity blocked with 5 μM NBQX + 50 μM APV and 5 μM NBQX + 50 μM APV + 100 μM PTX at day 21. One cell was recorded from each of three independent experimental replicates. Electrophysiology recordings were obtained from three biological replicates. Data are presented as means ± SEM.

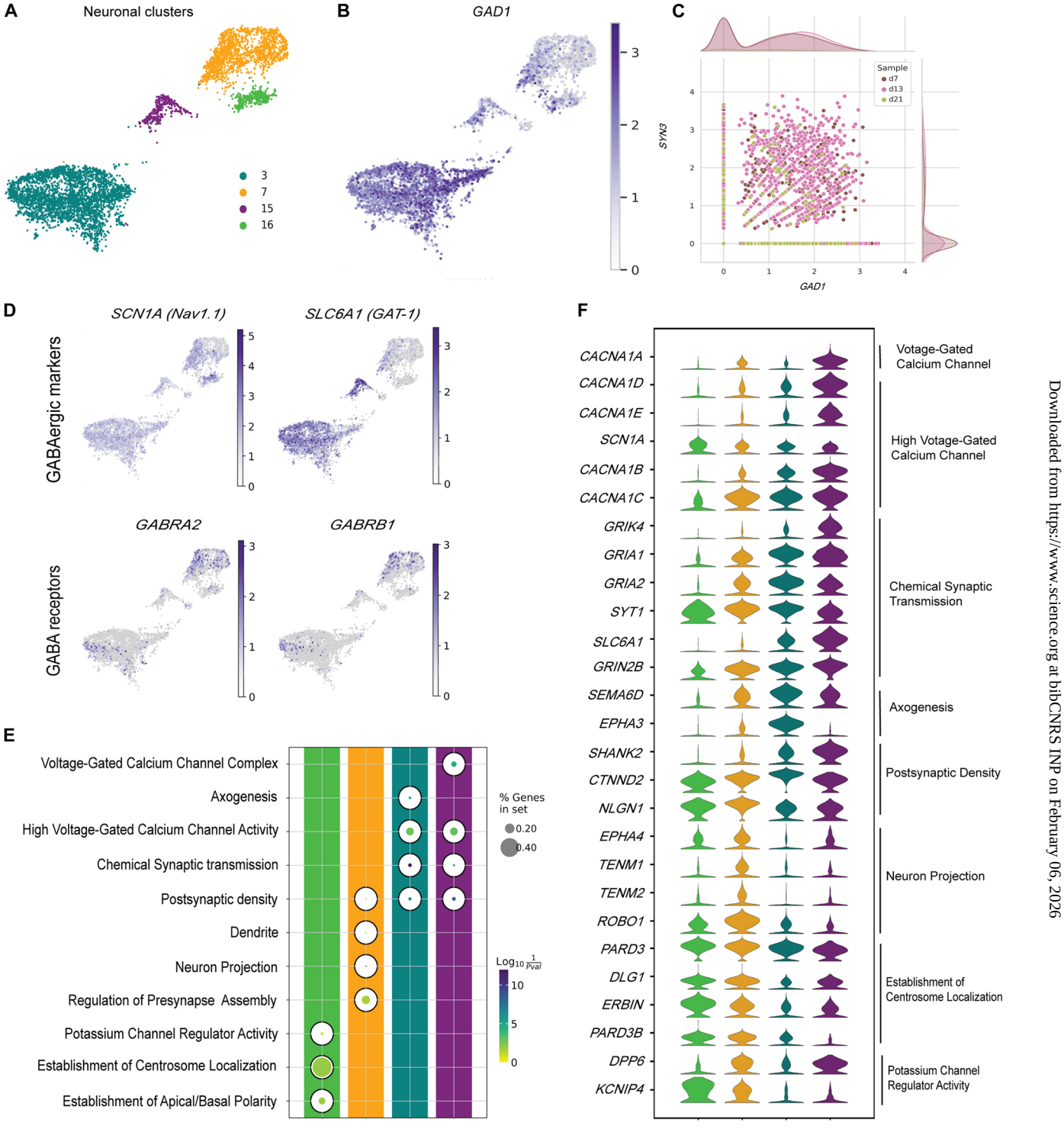

Fig. 4. Rapid induction into pallidal GABAergic neurons with mature neuronal signaling. (**A**) UMAP plot visualizing the neuronal clusters. (**B**) UMAP plot showing the expression of *GAD1* in neuronal clusters. (**C**) Scatterplot of cells coexpressing *GAD1* and *SYN3* in neuronal clusters. The numbers on the axis are the gene expression values, and the curves show the distributions of dots with different gene expression values. (**D**) UMAP plots demonstrating the expression levels of pan-GABAergic markers and GABA receptors (see also fig. S4). (**E**) Pathway analysis of neuronal clusters. (**F**) Violin plot showing differentially expressed genes in the four neuronal clusters.

Moreover, we could confirm an MGE-derived pallial fate by the expression of MAF BZIP Transcription Factor (*MAF*) and Neurexophilin 1 (*NXPH1*) (*29*) (day 13: 15.4 and 39.2% respectively; fig. S4A). There was no expression of cholinergic genes, including LIM Homeobox 8 (*LHX8*) and Choline O-Acetyltransferase (*CHAT*), marking interneurons of lateral ganglionic eminence (fig. S4B). These data support a neural induction of GABAergic pallidal fate with characteristic receptor genes.

After confirming a GABAergic phenotype for the reprogrammed neurons, the four clusters were further examined for transcriptional GSEA pathway analysis. Cluster 16 was enriched in pathways of centrosome localization, apical/basal polarity, and potassium channel activity but not for neuronal mature pathways (Fig. 4D). Cluster 7 was instead enriched in pathways involved in the regulation of presynaptic assembly, neuron projection, dendrite, and postsynaptic density (Fig. 4D). Clusters 3 and 15 showed the most mature neuronal pathways activation, e.g., those involved in chemical synaptic transmission and high voltage-gated calcium channel activity. Specifically, the purple cluster showed up-regulation of pathways related to voltage-gated calcium channels.

GSEA results were further confirmed by investigating the genes involved in these pathways (Fig. 4F). Analysis revealed differential expressions of the centrosome localization genes in the lime cluster, e.g., Par-3 Family Cell Polarity Regulator (*PARD3*), Discs Large MAGUK Scaffold Protein 1 (*DLG1*), *Erbb2 Interacting Protein* (*ERBIN*), and Par-3 Family Cell Polarity Regulator Beta (*PARD3B*) (*46*–*48*). Centrosome is a microtubule-organizing center, playing an important role in neuronal development and migration (*49*). These genes were still expressed in clusters 7 and 15, but here also postsynaptic density proteins, such as Catenin Delta 2 (*CTNND2*), *NLGN1*, and Multiple Ankyrin Repeat Domains 2 (*SHANK2*) were expressed (Fig. 4E). Cluster 7 showed up-regulation of neuronal migration and axon guidance genes, such as Teneurin Transmembrane Protein 1 and 2 (*TENM1* and *TENM2*), Roundabout Guidance Receptor 1 (*ROBO1*), and EPH Receptor A4 (*EPHA4*) (*50*, *51*), indicating migratory neurons. In clusters 3 and 15, presynaptic genes, i.e., Synaptotagmin 1 (*SYT1*) and *SLC6A1* and postsynaptic receptors, i.e., *GRIA1-2*, and *GRIN2B*, were more enriched, suggesting synaptically more mature cells. Cluster 3 was also enriched in axogenesis genes Semaphorin 6D (*SEMA6D*) and EPH receptor A3 (*EPHA3*) (*50*, *51*). The expression of both synaptic and migration genes strongly suggests the presence of immature neurons in this cluster. The genes encoding for Calcium Voltage-Gated Channel Subunit Alpha1 A-E (*CACNA1A-E*) were up-regulated specifically in cluster 15. This encodes for the P/Q-type calcium channel, which facilitates the fast GABA release from PV interneurons (*52*) and was further highlighted in UMAP, alongside the expression of Calcium Voltage-Gated Channel Auxiliary Subunit Gamma 5 (*CACNG5*) and Potassium Voltage-Gated Channel Interacting Protein 1 (*KCNIP1*) (fig. S4C).

Together, these data indicate neuronal signaling in the four neuronal clusters that are of different developmental stages, corroborating the gene expression patterns observed in Fig. 2G. Cluster 15, in purple, demonstrates a more mature profile with PV characteristic receptor genes critical for their phenotype.

Reprogrammed cells show transcriptional equivalence to interneurons, including PV chandelier neurons

To further explore the GABAergic phenotypes in the reprogrammed cells, we analyzed the expression of subtype-specific genes in the neuronal clusters. Noticeably, *PVALB* was a prominent subtype-specific marker and specifically enriched in the purple cluster (Fig. 5A). Other subtype-specific markers (e.g., *SST*, *CALB1*, and *VIP*) were also expressed (fig. S5A and table S7, *PVALB: 54*, *SST: 5*, *CALB1: 49*, *VIP: 13*, and *CALB2: 69* of *MAPT*+ cells at day 13). The *PVALB*-expressing cells were further explored for the three distinct categories: striatal, cortical chandelier, and cortical basket interneurons, characterized by specific marker expression (*53*–*57*). Results showed that most PV cells expressed characteristic chandelier subclass genes, with 50% *PVALB* coexpression with Fibroblast Growth Factor 13 (*FGF13*), 30% coexpression with Signal Peptide, CUB Domain And EGF Like Domain Containing 3 (*SCUBE3*), and 70% coexpression of RAR Related Orphan Receptor A (*RORA*). No PV cell coexpressed the striatal marker Parathyroid Hormone Like Hormone (*PTHLH*), and a few coexpressed basket subclass gene Extracellular Sulfatase Sulf-1 (*SULF1*), Semaphorin 3E (*SEMA3E*), and Gamma-Aminobutyric Acid Type A Receptor Subunit.

To test whether the induced PV interneurons were equivalent to bona fide human primary interneurons, we integrated and compared our dataset with a recently published dataset of cortical fetal and adult human interneurons (*40*) (Fig. 5C and fig. S5B). For this, we focused on the lime, yellow and purple clusters that showed more coherent transcriptomes required for proper integration. Cluster 3 could not be integrated due to high heterogeneity (likely due to a mix of mature and immature neurons). Using the top 50 harmony-adjusted principal components, we compared the reprogrammed interneurons with the human endogenous interneurons (*40*). This comparison resulted in 100 reprogrammed cells having a cosine similarity score higher than 0.8 of 1 for the PV clusters (PV and PV_MP) (Fig. 5D and fig. S5C), highlighting transcriptional similarity to the endogenous PV branch (see table S8 for list of genes with high similarity). Moreover, we identified the most similar primary neurons for the yellow cluster to be "Interneurons" (INT) and for the lime cluster to be "Progenitors" reaching cosine similarity scores of 0.8 of 1 (Fig. 5D and fig. S5C, cluster 7: 1600 cells, cluster 16: 381, and subcluster of 15: 140 mature cells). These results demonstrate that human-reprogrammed PV interneurons exhibit transcriptional profiles comparable to those of primary PV interneurons and that the remaining neuronal clusters resemble interneurons and progenitor populations.

The interneuron phenotype was next confirmed with immunocytochemistry (Fig. 5E). Although GABA protein expression was low in the ND and GM controls, it was drastically increased in the ADLSF condition at day 21 (Fig. 5E). There was a strong induction in PV protein levels exclusively in the ADLSF condition, confirming a PV phenotype and the necessity for exogenous applied transcription factors for its conversion (Fig. 5E).

To reduce the viral load on hGPCs and assess the necessity of all five transcription factors for reprogramming, we also tested conversion using a reduced set of factors (ADL). Nevertheless, this approach did not achieve PV reprogramming efficiency comparable to the full ADLSF combination (fig. S5D), indicating that the complete ADLSF set yields superior outcomes.

The ADLSF-induced PV cells were detected throughout the entire 3D spheroid structure (assessed by analyzing *z*-stacks from confocal imaging), demonstrating homogeneous PV reprogramming within the 3D structure (Fig. 5F). PV cells showed colocalization with the mature neuronal marker TAU (Fig. 5G) and manifested a complex neuronal phenotype with distinct dendritic trees within the spheroid structure (Fig. 5H and movie S1), implying a mature neuronal

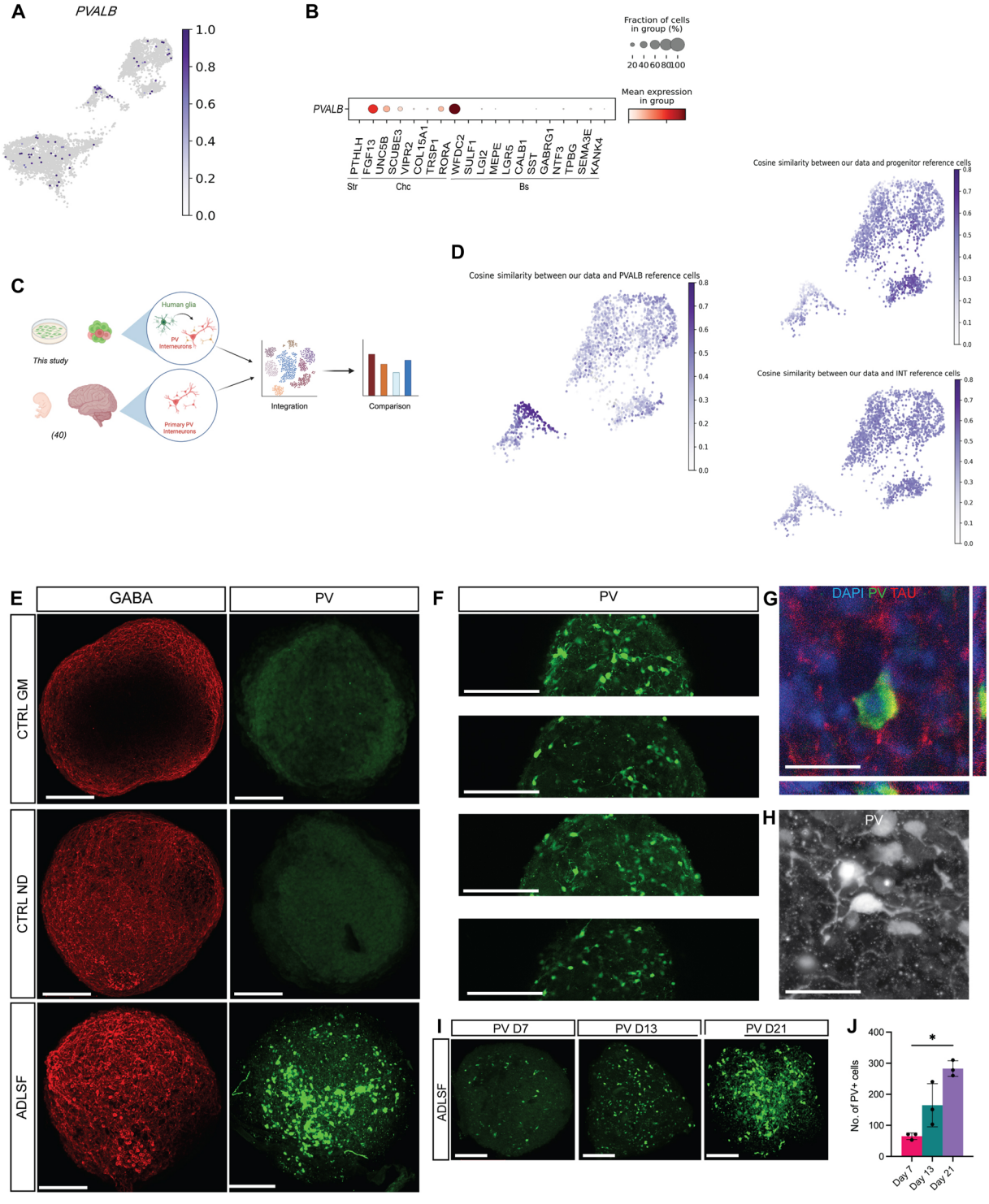

Fig. 5. Reprogramming into interneurons with transcriptional equivalence to interneurons, including PV chandelier neurons. (**A**) UMAP plot of expression levels of *PVALB* (see also fig. S5A). (**B**) Dot plot showing the expression of subclass-specific markers for reprogrammed PV cells. (**C**) Schematic overview of the integration and comparison process with a published dataset (*40*) (see also fig. S5B). (**D**) UMAP plots of cosine similarity score between reference PV clusters, Interneuron cluster, and progenitor cluster of a published dataset (*40*) and the neuronal clusters of this study (see also fig. S5C). (**E**) Maximum intensity projections of immunostaining of GM and ND controls and induced neuron spheroids with GABA and PV at day 21 (see also fig. S5D). (**F**) Different *z*-stacks of immunostaining of PV and its distribution throughout the whole spheroid at day 21. (**G**) Immunostaining of PV and pan-neuronal marker TAU in 3D spheroids at day 21. (**H**) 40X picture confocal image of a single PV interneuron at day 21 (see also movie S1). (**I**) Representative images of immunostaining of PV cells at days 7, 13, and 21. (**J**) Quantification of PV cells at days 7, 13, and 21 ($n = 3$, n = biological replicate): $^*P < 0.05$, Kruskal-Wallis test with uncorrected Dunn's test. Scale bars, 100 μm (F) and 40 μm [(I) and (J)]. Each dot represents a biological replicate. Data presented as means ± SEM.

phenotype. To observe the potential changes in PV protein expression over time, we manually quantified the PV cells on days 7 to 21. Results showed a gradual increase over time, reaching 283 ± 25 PV cells per spheroid (Fig. 5, I and J), suggesting a continuous survival and potential increase in PV protein, or cell numbers when maintained in 3D culture (as opposed to nuclei isolation where mature neurons are prone to damage). In line with this, RT-qPCR analysis showed a clear up-regulation of the pan-GABAergic marker Solute Carrier Family 32 Member 1 (*SLC32A1* or *VGAT*) and the interneuron subtype-specific marker *PVALB* (fig. S5E). Although there was a small induction of *SST* and *CALB1* genes (fig. S5E), the expression levels were lower compared to the *PVALB* gene and could not be detected on the protein level.

Together, these data demonstrate successful human glial-to-PV reprogramming at both the transcriptional and protein levels and show that the process occurs homogeneously throughout the 3D structure.

Constructing the lineage trajectory of reprogrammed PV chandelier interneurons

To further understand the glia-to-PV conversion, we examined the cellular transcriptomic trajectory using latent time reconstruction of the snRNA-seq data. We based this on RNA velocity (*58*) and PAGA analysis (*59*) with Fig. 2B as a backbone. Latent time was used to trace cell maturity from a "branching point," i.e., glia cluster (red cells in Fig. 6A) to the PV cluster (dark blue cells in Fig. 6A) with RNA velocity analysis and PAGA analysis (fig. S6, A and B). This analysis resulted in the generation of two distinct lineage trajectories. The left trajectory did not reach the PV cluster but instead led to other clusters (including cluster 1 and 3), and was therefore designed as "non-PV trajectory" (black arrows in Fig. 6A), whereas the right trajectory successfully reached the PV cluster and was defined as the "PV trajectory" (blue arrows in Fig. 6A).

To corroborate these findings from latent time–RNA velocity analysis, we performed diffusion pseudotime analysis (*59*), which is based on changes in gene expression similarity (Fig. 6B). Here, we were able to identify the three clusters involved in the good trajectory on the diffusion map (Fig. 6C), corresponding to the ones of the UMAP (Fig. 6A and fig. S6A). The cells within the PV trajectory (Fig. 6E) appeared interconnected in the diffusion map, with the end of the cluster showing the highest level of maturity, indicated by the blue color in Fig. 6D.

To identify a potential glial subpopulation most connected to the "PV trajectory," we analyzed cells of day 0 to day 1 using subclustering and PAGA analysis. This showed a distinct cluster (pink cells in fig. S6B) that was different from the initially dedicated glia cluster (red cluster in Fig. 6A). The gene profile in these cells only existed up until day 1 (fig. S6B), indicating rapidly changing genes. Next, we examined the expression of glial markers in the reprogrammed cells (fig. S6C), and could observe that pathway diversification did not appear to depend on the specific phenotype of the starting glial population, as cells at day 0 to 1 expressed a wide range of glial markers.

In addition, there was a strong connectivity between the day 7 to 13 neuronal cluster and the day 21 cluster (fig. S6D; cluster 3-1 from Fig. 2F), implying that day 21 cells arise from reprogrammed neurons reverting to an immature or "confused" state, representing the terminal cellular state of the trajectory.

We next selected genes from the top 100 DEGs in the clusters of the "PV trajectory," plotted against latent time (see Fig. 6F), to unravel critical genes in the PV trajectory. The heatmap demonstrated a gradual down-regulation of genes associated with hGPC identity, such as Mastermind Like Transcriptional Coactivator 2 (*MAML2*), *PTPRZ1*, SRY-Box Transcription Factor 6 (*SOX6*), and GLIS Family Zinc Finger 3 (*GLIS3*) (*39*). Conversely, there was an increase in the expression of mature neuronal markers, e.g. *NTM*, Opioid Binding Protein/Cell Adhesion Molecule Like (*OPCML*), RNA Binding Fox-1 Homolog 3 (*RBFOX3*), and Synaptosome Associated Protein 25 (*SNAP25*), signifying the transition toward a neuronal fate. Notably, there was transient up-regulation of progenitor genes, e.g. NK2 Homeobox 1 (*NKX2-1*) (*60*), neuronal migration genes, e.g. Pleckstrin Homology, RhoGEF Domain Containing G1 (*PLEKHG1*). Moreover, the gene WW Domain Containing Oxidoreductase (*WWOX*) was gradually up-regulated (Fig. 6F), as were postsynaptic proteins gephyrin (*GPHN*) and *NLGN1*. Toward the end of the latent time, genes involved in the PV transcriptional profile also came up, e.g., PPARG Coactivator 1 Alpha (*PPARGC1A*), Estrogen Related Receptor Gamma (*ESRRG*), and *RORA*.

We then plotted the same genes on a heatmap for the clusters that are not part of the "PV trajectory" (Fig. 6G). The heatmap clearly demonstrated no or very low expression in these clusters compared to clusters involved in the PV trajectory. This indicates that the selected genes in Fig. 6F show distinct expressions pattern in the good trajectory, highlighting their importance in the PV fate specification, especially during glial reprogramming.

Certain genes in the heatmap were dynamically expressed over time, with some rapidly down-regulating (*PTPRZ1*), or exhibiting more dynamic expression patterns (*NKX2-1*) (Fig. 6H). There was a robust up-regulation of *WWOX*, *RORA*, and *RBFOX3* as early as day 7, which, together with the fast PV induction, corroborated the fast gene dynamics in the glia-to-PV conversion (Fig. 6H).

Notably, the expression of each transgene (ADLSF), and the proportion of transduced cells, were higher in the "PV trajectory" compared to the non-PV trajectories (fig. S6, E and F). A higher fraction of cells expressing all transcription factors was observed for all factors except *LHX6*. In particular, 61% of cells transduced with *Ascl1* and 55% of cells transduced with *DLX5* were found in the PV trajectory. Furthermore, 44% of *LHX6*-transfected cells, 68% of *Sox2*-transfected cells, and 69% of *FOXG1*-transfected cells were part of the PV trajectory further supporting the pivotal role of these reprogramming factors in the PV fate acquisition.

In summary, these results unravel a distinct glia-to-neuron lineage pathway where cells progress through different stages, obtaining the necessary machinery for synaptic communication and energy demand to ultimately attain a complete PV neuronal fate.

The discovery of distinctly expressed transcription factors in the PV trajectory can have functional implications for further PV derivations. We chose to manipulate one of them—*RORA*, highly expressed on day 7—in vitro to potentially increase the PV yield. *RORA* transgene was delivered into a doxycycline-regulated lentiviral vector and added to the reprogramming cocktail (ADLSF+R) with successful expression in reprogrammed PV neurons (fig. S7A). Transduction of ADLSF+R did not impair the induction of complex PV neuron morphology but appeared to induce longer segments (fig. S7, B and C). Nevertheless, the TAU and PV yield remained similar (fig. S7D; 40.7 and 6.8% respectively) to the ADLSF condition (49.8 and 4.4%, respectively), indicating no effect on PV yield but increased the complexity of PV cells. RT-qPCR analysis showed a trend of increased *SYN1* and *VGAT* expression along with a small but confirmed increase in *PVALB* gene expression (fig. S7E). Yet, PV protein was seen at similar levels in both conditions (fig. S7, F and G).

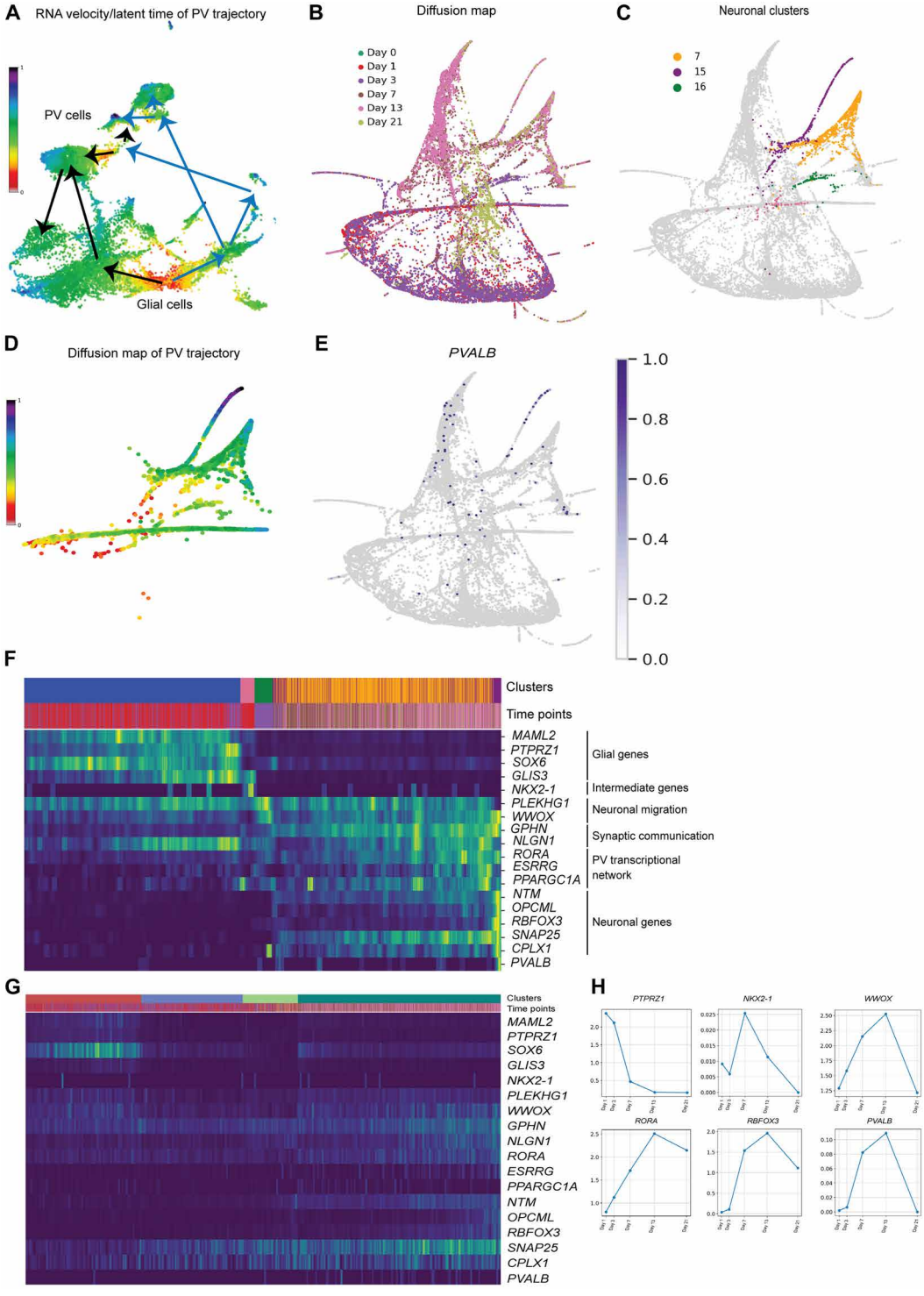

Fig. 6. Constructing the lineage trajectory of reprogrammed PV chandelier interneurons. (**A**) UMAP visualizing the reconstructed reprogramming trajectory on latent time (see also fig. S6, A to D). (**B**) Diffusion map with all time points. (**C**) Representation of the corresponding neuronal clusters on the diffusion map. (**D**) Representation of the reconstructed PV trajectory of the diffusion map colored by latent time. (**E**) Diffusion map showing PV-expressing cells. (**F**) Heatmap visualizing important genes of the PV trajectory. (**G**) Heatmap visualizing the same genes of the non-PV trajectory. (**H**) Average expression of specific genes at different time points of reprogramming.

Overall, these data suggest that ectopically delivered *RORA* does not affect the overall number of PV cells but has the potential to increase neuronal complexity and enhance PV gene expression.

DISCUSSION

GABAergic interneurons exert unique properties of precise regulation in local circuitry, brain networks, and memory processing (*22*). The chandelier PV interneurons specifically control the firing rate of pyramidal cells and cortical gamma oscillations (*61*) and their dysfunction is associated with several neurological disorders characterized by network alteration and cognitive impairment, e.g., autism spectrum disorders, schizophrenia, epilepsy, and Alzheimer's disease (*23*–*27*, *62*).

Interneuron transplantation has shown to mitigate disease pathology and even reopen the critical window of cortical plasticity (*3*, *63*). Still, generating PV interneurons from stem cells or fetal tissue remains challenging, potentially due to their extensive developmental timelines and limited availability of human fetal tissue (*3*, *32*). Direct reprogramming offers a promising alternative, enabling the conversion of patient-specific glial cells into neurons via ectopic expression of neural genes. This strategy bypasses the pluripotent stages linked to tumorigenicity (*2*) and is therefore particularly suited for in vivo applications, especially with recent advances in viral vector technology allowing for noninvasive delivery across the blood-brain barrier (*2*).

Direct neuronal reprogramming of glial cells might be especially advantageous for interneuron generation, given their shared developmental origins and permissive chromatin states (*16*). As expected, glia-to-interneuron generation has been proven effective in rodent models (*4*–*10*) but its feasibility in human glia remains to be fully explored.

Herein, we have established a human glia reprogramming approach into interneurons with molecular features of PV interneurons. Stem cell–derived hGPCs were transduced with a combination of transcription factors determining GABAergic fate (*20*, *34*) in a 3D spheroid approach, designed for increasing communication and viability over an extended timeline (*37*). Under these conditions, the hGPCs efficiently converted into neurons and exhibited marked biomolecular changes as seen with label-free biospectroscopic analysis. As one of the biospectroscopic applications on reprogrammed neurons, our results revealed a consistent and widespread induction of a new cell type distinct from the original glial progenitors, with changes evident throughout the entire spheroid structure. These findings were further supported by molecular data, including a robust and rapid up-regulation of the *PVALB* gene and PV protein expression detected as early as 7 days posttransduction, confirmed by single-nucleus transcriptomic analysis. Although pallial interneurons have previously been generated from human stem cells in vitro, or via reprogramming approaches in mouse brains (*4*–*10*, *32*, *33*), this study demonstrates the generation of human PV subtype interneurons of in vitro (*20*).

Whereas glia cells during development include both neural stem cells and progenitor cells, this population is considered to be lineage-restricted in the adult mammalian brain (*64*). Yet, GPC cells do seem to have potential for lineage transmission when exposed to different environments, e.g., in vitro (*64*). The fact that our hGPCs (both at day 0 and in controls) showed expression of *DCX* and some *SYN1* supports a neurogenic potential of the GPC population also in our 3D in vitro environment. Nevertheless, the conversion to mature neurons with interneuron phenotype was all dependent on ADLSF transduction and not due to spontaneous glia-to-neuron differentiation, as confirmed by the GM and ND control conditions.

Induced neurons and PV cells were herein uniquely analyzed for their full transcriptomic profile. When comparing this to a previously published dataset of cortical fetal and adult human interneurons, we found a high similarity between the induced and authentic interneurons, neuronal progenitors, and PV chandelier cells. Specifically, the gene expression patterns of our best-matching cells showed up to 80% similarity to the endogenous cortical PV chandelier cells. This level of resemblance has been seen in previous comparisons of stem cell–derived SST interneurons (*65*, *66*) and showcases the ability of our reprogramming paradigm to reach a highly authentic cell product. Moreover, it confirms the attainment of a mature state within only 2 weeks using ectopic expression of transcription factors, as opposed to months required for stem cell differentiation or in vivo development (*29*–*32*).

Little is understood about reprogramming dynamics and how this rapid and drastic process occurs in terms of transcriptional regulation (*67*). To understand the gene dynamics during neuronal reprogramming, we further assessed the transcriptomic shift from glia-to-PV interneurons as a first attempt using hGPCs. Our trajectory analysis revealed two distinct routes of hGPCs upon initiation of the reprogramming process: one route led to transcriptionally mature bona fide PV interneurons, whereas the other resulted in unsuccessful PV interneuron reprogramming, with cells converting to an immature GABAergic state. This pathway still showed distinct transcript to day 0 and GM control, with expression of neuronal transcript that could be confirmed with neuronal signaling pathway and functional maturity data, thus supporting a glia-to-neuronal switch even in the non-PV pathway. The presence of two distinct routes might indicate heterogeneity in the system, possibly influenced by the stochastic uptake of each transcription factor and their expression levels or the reprogramming potential of the starting cell population (*67*). Nevertheless, these hGPCs have previously shown similar neuronal conversion rates regardless of the starting glial types, suggesting equal reprogramming potential (*37*). We might also have diversification in upstream states from the starting cell, as additional complexity to the decisional route toward the PV state.

We herein reveal the dynamic expression of several genes for PV fate acquisition, whose relevance is previously unknown in the context of human reprogramming. Among these, we observed transient up-regulation of neuronal migration genes such as *PLEKHG1* and *WWOX*, possibly reflecting a more accessible chromatin around these genes and the migratory nature of hGPCs. *PLEKHG1* is necessary for proper cortical migration of MGE progenitors linked to (*68*), which have been implicated in neurogenesis and neuronal migration (*69*, *70*). Notably, *WWOX* also emerged as an intermediate gene in this trajectory. This protein is highly expressed in basket PV cells (*71*) and its ablation leads to a significant hippocampal reduction of PV interneurons (*72*) or impairments in neuronal differentiation and migration (*73*). Our data also support a transient up-regulation of progenitor genes, e.g., *NKX2-1*, in the reprogramming pathway, as previously observed (*67*).

In addition to these factors, also postsynaptic proteins *GPHN* and *NLGN1* were transiently up-regulated in our glia reprogramming. *GPHN* is a puncta marker for inhibitory synapses and a master regulator for chandelier-mediated transmission (*74*) and *NLGN1* is expressed at excitatory synapses supporting NMDA receptors

modulating excitatory transmission (*75*). This corroborates the up-regulation of postsynaptic glutamate and GABA receptors observed in the neuronal clusters and suggests that the reprogrammed cells express necessary synaptic machinery for both excitatory and inhibitory signals. Also, markers of mitochondria biogenesis and metabolism, e.g., *PPARGC1A*, *ESRRG*, and *RORA* were seen transiently up-regulated. These genes are believed to orchestrate a PV-specific transcriptional network (*45*, *76*) and, to our knowledge, have not yet been reported in the context of human neuronal reprogramming. Together, our data suggest that human glia reprogramming progresses through different neuronal developmental stages and includes the establishment of the necessary synaptic machinery and communication, as well as adjustments for energy demand (*77*), to acquire a complete PV neuronal fate.

In our protocol, RORA demonstrated some potential to increase *PVALB* gene expression and neuronal complexity of the PV interneurons, providing a proof of concept that an extrinsically delivered gene can affect fate specification and maturation during reprogramming. Whereas *RORA* has previously been implicated in orchestrating a transcriptional network supporting the metabolic needs of PV interneurons (*45*), more studies are still needed to fully evaluate the effects of *RORA* on PV reprogramming or stem cell differentiation.

The converted glia in our protocol underwent functional neuronal maturation when kept in long-term culture, in both passive and active properties. These data were further supported by the single-nuclei sequencing data, with up-regulation of genes encoding membrane receptors that control synaptic function and voltage-gated sodium and potassium channels, such as *SCN1A* and *CACNA1A*. Of note, the most mature clusters appeared on day 7 to 13, whereas day 21 cluster showed immature neuronal, "confused cells" similar to ND control corresponding to the end trajectory state (fig. S6). This potential drawback of the protocol is likely due to a bias toward immature cells that survive the nuclei extraction procedure for snRNA-seq and the fragility of the mature neurons to remain, even in 3D cultures (*37*). Despite the neuronal maturation, sodium and potassium currents recorded in these cells at day 50 remained small compared to those recorded from stem cell–derived GABAergic neurons, suggesting that the cells are still functionally immature and may not yet have the full repertoire of membrane channels required for the PV characteristic fast-spiking behavior. A high density of sodium channels in the axon and potassium channels with a high activation threshold and fast deactivation are crucial for the temporal precision and frequency of AP firing in PV interneurons. Therefore, it is likely that such sophisticated properties can only be acquired once the cells integrate into a proper neuronal circuit in vivo (*78*).

In conclusion, we herein demonstrate a rapid and reproducible lineage reprogramming of human glial precursor cells into neurons of therapeutic relevance for neurological disorders. In this process, we revealed the first glia lineage transition dynamics and identified several genes involved with potential implications for future protocols toward PV interneurons. This shows a proof of concept of human glia reprogramming into interneurons and holds potential for future cell engineering strategies for brain disorders affecting interneurons and circuitry repair.

Limitations of the study

We use a recently established 3D human culture system that facilitates better communication between cells and supports prolonged cell viability over time. Despite the advantages of this system, it does not fully replicate the human brain environment as key inputs (i.e., glutamatergic), are absent, and current technology limits automated cell quantification. Further studies and efforts are needed to fully assess the functional maturation and integration of these reprogrammed neurons into an in vivo environment. Moreover, we applied RNA velocity to our snRNA-seq data, to assess the lineage trajectory, even though RNA velocity was originally designed for single-cell RNA-seq data. To address this issue, we used an extra trajectory inference method, which corroborated the results obtained from RNA velocity, and showcases the robustness of the velocities. Last, although this study shows two different reprogramming trajectories, it does not further explore the mechanism of bifurcation. Future studies should investigate this by, i.e., designing polycistronic constructs or sorting the starting cell population to identify a subpopulation more prone to GABAergic reprogramming. Fourth, this study generates a limited number of functionally mature subtype-expressing interneurons that might prevent deciphering the full reprogramming trajectory.

MATERIALS AND METHODS

Stem cell–derived GPCs production

hGPCs were obtained from hESCs (RC17 Roslin Cells, catalog no. hPSCreg RCe021-A, p26–30). hESCs were cultured on tissue plates coated with LN521 (0.5 μg/cm^2; Biolamina, Sundbyberg, Sweden) and kept in IPS-Brew XF medium (StemMACS, Miltenyi, Bergisch Gladbach, Germany). Weekly passages were performed using EDTA (0.5 mM, Gibco, Thermo Fisher Scientific, Waltham, MA, USA). hESCs were differentiated into hGPCs according to established protocols (*18*).

Lentiviral production

Previously described vectors (*20*) were used for the direct conversion of hGPCs. Briefly, we used a mix of constitutively expressed and doxycycline-dependent transcription factors. The constitutively regulated transcription factors were open reading frames (ORFs) of *Ascl1*, *DLX5*, and *LHX6*. The doxycycline-regulated transcription factors were ORFs of *Sox2* and *FOXG1*. All the transcription factors were in third-generation lentiviral vectors (LVs). hGPCs were always cotransduced with LV containing the FUW-M2rtTA plasmid (#20342, Addgene, Watertown, MA, USA) for the expression of doxycycline-regulated transcription factors. The lentiviral vector used to overexpress *RORA* (pLV [Exp]-EGFP-TRE>hRORA with vector ID VB230913-1017xen) was constructed and packaged by VectorBuilder. LVs were produced as previously described (*79*) and titrated with qPCR analysis. The range of the titers was 2.5×10^8 to 3.4×10^9.

Conversion of hGPCs and generation of converted spheroids

At 2 to 3 weeks after thawing, hGPCs were detached with a cell scraper and dissociated into single cells with Accutase (StemPro, Thermo Fisher Scientific; Waltham, MA, USA). A total of 100,000 single hGPCs were mixed with the lentiviral reprogramming cocktail [multiplicity of infection (MOI) of 1 to 2 per vector] in 60 ml of media and seeded in 96-well U-bottom plates (#CLS7007, Corning, NY, USA) for self-aggregation. After 24 hours, 60 μl of fresh medium containing doxycycline (5 μg/ml; Duchefa, Haarlem, Netherlands) was exchanged to induce tet-regulated transgene expression. Three days after transduction, the medium was replaced by ND medium, which consisted of NDiff227 (Takara-Clontech, Gothenburg, Sweden), with doxycycline (5 μg/ml for 3D and 2 μg/ml for 2D), small

molecules [CHIR99021 (2 μM, Axon, Groningen, Netherlands), SB-431542 (10 μM, Axon, Groningen, Netherlands), noggin (0.5 μg/ml; R&D Systems, Minneapolis, MN, USA), and LDN-193189 (0.5 μM, Axon, Groningen, Netherlands), VPA (1 mM, Merck Millipore, Burlington, MA, USA)] and growth factors [LM-22A4 (2 μM, R&D Systems, Minneapolis, MN, USA), GDNF (2 ng/ml; R&D Systems, Minneapolis, MN, USA), NT3 (10 ng/ml; R&D Systems, Minneapolis, MN, USA), and db-cAMP (0.5 mM, Sigma-Aldrich, St. Louis, MO, USA)]. The ND medium was exchanged every 2 to 3 days. Small molecules and doxycycline were withdrawn from the medium after 2 weeks to promote maturation of the neurons. The converted spheroids were kept in the ND medium supplemented with growth factors, partially exchanged every 2 to 3 days, until the termination of the experiment. For 2D conversion, 24-well plates (Costar, Corning, USA) were serially coated with polyornithine (15 μg/ml; Sigma-Aldrich, St. Louis, MO, USA), laminin (5 μg/ml, Gibco, Thermo Fisher Scientific, Waltham, MA, USA), and fibronectin (0.5 ng/μl, Gibco, Thermo Fisher Scientific, Waltham, MA, USA). A total of 100,000 single hGPCs were seeded, and after 24 hours, they were transduced at MOI 1 to 2. After 24 hours, 500 μl of GM supplemented with doxycycline (2 μg/ml, Duchefa) was exchanged for activation of tet-regulated transgenes. The same medium was used as in 3D cultures.

Fluorescence-activated cell sorting analysis

Two to three weeks after thawing, hGPCs were analyzed using fluorescence-activated cell sorting (FACS). Briefly, cells were mechanically detached and dissociated with Accutase (StemPro, Thermo Fisher Scientific; Waltham, MA, USA) for 8 min and were resuspended in Miltenyi wash buffer [phosphate-buffered saline (PBS), Gibco, Thermo Fisher Scientific; Waltham, MA, USA; 0.5% BSA Fraction V Gibco, Thermo Fisher Scientific; Waltham, MA, USA; 2 μM EDTA; and 0.05‰ (per mil) Phenol Red, Sigma-Aldrich, St. Louis, MO, USA] in a concentration of 1×10^6 cells/ml. This was followed by incubation with fluorochrome-conjugated antibodies [PE anti-human CD140a (BD Biosciences, catalog no. 556002, Eysins, Switzerland 1:10), APC anti-CD44 (Miltenyi, catalog no. 130-113-331, Bergisch Gladbach, Germany, 1:100), APC anti-human CD133/1 (Miltenyi, catalog no. 130-113-668, Bergisch Gladbach, Germany, 1:50), and FITC anti-human SSEA-4 (BioLegend, catalog no. 330410, Bergisch Gladbach, Germany, 1:20)] for 15 min at 4°C and washed in wash buffer for 10 min at 200*g*. Subsequently, cells were transferred into prewet 5-ml polystyrene tubes with cell-strainer caps with propidium iodide (PI; Miltenyi, catalog no. 130-095-177, 1:500, Bergisch Gladbach, Germany) to exclude dead cells. A total of 10,000 events were analyzed on a FACSAria III sorter (BD Biosciences, Eysins, Switzerland). Gates were set on Fluorescence Minus One (FMO) control, and compensation was performed with single-stained cells.

RNA extraction, cDNA synthesis, and RT-qPCR

Spheroids were lysed with RLT buffer (Qiagen, Hilden, Germany), and total RNA extraction was performed using RNeasy Micro Kit (Qiagen, Hilden, Germany) following the manufacturer's protocol. Subsequently, RNA was reverse-transcribed to cDNA using the Maxima First Strand cDNA Synthesis Kit (Thermo Fisher Scientific, Waltham, MA, USA) according to the manufacturer's protocol. The RT-qPCR mix was premixed using the Bravo Automated Liquid Handling Platform (Agilent, Santa Clara, CA, USA). cDNA (1 μl) was mixed with LightCycler 480 SYBR Green I Master (5 μl, Roche, Basel, Switzerland) and relevant primers (4 μl, Eurofins Genomics, Luxembourg City, Luxembourg; see table S3) in three technical replicates for each sample. RT-qPCR was performed in a LightCycler 480 II instrument (Roche, Basel, Switzerland) using a 40-cycle two-step PCR protocol (95°C, 30-s denaturation and 60°C, 1-min annealing/elongation). Analysis was performed from technical triplicates, and the relative gene expression was calculated using the comparative CT Method (ΔΔCT Method), and every sample was compared to hGPCs before lentiviral transduction. Expression was normalized against the housekeeping genes *GAPDH* and *ACTB*.

Whole spheroid immunostaining with optical clearing and 2D immunostaining

Whole spheroid immunostaining and optical clearing were performed according to (*80*). Briefly, converted and control spheroids were fixed using 4% paraformaldehyde (PFA) or a mixture of 4% PFA and 0.25% glutaraldehyde (catalog no. G6257, Sigma-Aldrich, St. Louis, MO, USA) for 20 min at room temperature (RT). An overnight incubation in blocking solution containing 5% donkey serum, 0.3% Triton X-100 (Sigma-Aldrich, St. Louis, MO, USA), and PBS followed. Incubation with primary antibodies diluted in blocking solution was performed for 24 hours at RT on a shaker (see table S4). This was followed by incubation with secondary antibodies conjugated to Alexa-488/Cy2, Alexa-568/Cy3, or Alexa-647 (1:200; Jackson ImmunoResearch Laboratories, West Grove, PA, USA) and DAPI (1:2000, Sigma-Aldrich, St. Louis, MO, USA) for 24 hours at RT on a shaker. Samples were then dehydrated in an ascending serial methanol concentration for 10 min each, and lipids were removed by incubation with a dichloromethane-methanol mixture for 1 hour, followed by two steps of 10-min incubation, each in dichloromethane. Last, spheroids were cleared with ethyl cinnamate and transferred to 96-well plates with flat and clear bottoms (Ibidi, Gräfelfing, Germany) for confocal microscopy.

For 2D immunostaining, cells were fixed with 4% PFA for 15 min at RT. Subsequently, cells were incubated in a blocking solution (5% donkey serum and 0.1% Triton-X 100 in PBS) for 1 to 3 hours. Cells were incubated with primary antibodies (table S4) diluted in a blocking solution overnight at 4°C. The next day, incubation with secondary antibodies and DAPI was performed for 1 hour at RT in the dark. Cells were kept at 4°C until microscopy.

Patch-clamp electrophysiological recording of reprogrammed spheroids

Whole-cell patch-clamp electrophysiological recordings were performed at 7, 13, 21, and 50 days posttransduction. Briefly, converted free-floating spheroids were recorded at RT in Krebs solution containing 119 mM NaCl, 2.5 mM KCl, 1.3 mM $MgSO_4$, 2.5 mM $CaCl_2$, 25 mM glucose, and 26 mM $NaHCO_3$ continuously gassed with 95% O2–5% CO_2. Borosilicate glass pipettes (5 to 7 MΩ) filled with the following intracellular solution: 122.5 mM K-gluconate, 12.5 mM KCl, 0.2 mM EGTA, 10 mM Hepes, 2 mM MgATP, 0.3 mM Na_3GTP, and 8 mM NaCl adjusted to pH 7.3 with KOH were used. Recordings were carried out with the Multiclamp 700B System (Molecular Devices), digitized at 20 kHz, and acquired with pClamp 10.6 (Molecular Devices). Pipette access resistance was monitored throughout the recording and was between 9 and 25 MΩ. Cells were selected on the basis of viability, neuronal shape, and clean access. Immediately after whole-cell configuration was established, RMP, Ri, and Cm were calculated from a series of 5-mV pulses of 100-ms duration. AP generation was examined by delivering a series of 500-ms

duration depolarizing steps starting from −20 to +35 pA with 5-pA increments at the current clamp, whereas the RMP of the cells was held at −70 mV by constant current injection. Peak amplitude and AHP of the first elicited AP were calculated as the voltage difference from the AP threshold. For inward sodium (Na+) and delayed rectifying potassium (K+) current measurements, cells were clamped at −70 mV, and 100-ms duration depolarizing steps were delivered starting from −70 to +40 mV with 10-mV increments at voltage clamp. To confirm the GABAergic nature of converted spheroids, APV (50 μM), NBQX (5 μM), and picrotoxin (100 μM) were added to the Krebs solution in the recording chamber. Igor Pro 8.04 (Wavemetrics), combined with the NeuroMatic package and Clampfit (Axon pClamp), was used for data analysis.

O-PTIR microspectroscopy

O-PTIR experiments were performed using the mIRage microscope (Photothermal Corp., Santa Barbara, USA) available at the SMIS beamline at the synchrotron SOLEIL (France). For these measurements, 20-μm-thick cryocut spheroids were directly deposited on a glass slide. The photothermal effect was detected by modulating the intensity of a continuous wave (CW) 532-nm laser, induced by an infrared laser. The probe power was set to 2.4%. Hyperspectral images were acquired by scanning from 3026 to 1000 cm^{-1} at an 80-kHz repetition rate using a 2 μm–by–2 μm step. Further details on the spectroscopic measurements of tissue can be found in a previous work (*81*). Data analysis was performed using the Quasar software for unsupervised analysis of spectra. Specifically, we focused on the lipid signature within the range of 3026 to 2800 cm^{-1}, the protein signature within the range of 1700 to 1500 cm^{-1}, and metabolites within the range of 1475 to 1300 cm^{-1}. The preprocessing of spectra involved cutting out the spectral part from 1300 to 1000 cm^{-1} to avoid glass sample support contribution, followed by baseline correction and min-max normalization. Spectra of poor quality (with high signal-to-noise ratio) were excluded using *k*-means clustering. Subsequently, principal components analysis (PCA) was used to investigate characteristic signatures.

Nuclei isolation and sorting

Spheroids were collected at different time points during the experiment, snap frozen on dry ice, and kept at −80°C until processed. Nuclei isolation was performed according to the following protocol (*82*) with modifications. Briefly, spheroids were thawed at 4°C and dissociated in ice-cold lysis buffer consisting of 0.32 M sucrose, 5 mM $CaCl_2$, 3 mM MgAc, 0.1 mM Na_2EDTA, 10 mM tris-HCl (pH 8.0), 1 mM dithiothreitol (DTT), 0.1% Triton X, EDTA-free proteinase inhibitor (Roche, Basel, Switzerland), and RNase inhibitors (Ambion and SUPERase·In, Invitrogen, Carlsbad, CA, USA). This was followed by centrifugation of the lysates for 30 min at 11,000*g*. The pelleted nuclei were resuspended in a buffer containing 0.1% BSA Fraction V, PBS −/−, RNase inhibitors (Ambion and SUPERase·In, Invitrogen, Carlsbad, CA, USA), and Draq7 (BD Biosciences, no. 564904, Eysins, Switzerland). The nuclei were filtered with a 70-μm cell strainer into bovine serum albumin (BSA)–coated DNA LoBind tubes (Eppendorf, Hamburg, Germany) for sorting. FACS was performed with a FACSAria cell sorter on a 100-μm nozzle and with the FACSDiva software (BD Biosciences, Eysins, Switzerland) on a low flow rate to separate single nuclei. A total of 10,000 nuclei were collected in each sample to a total volume of 20 μl and directly processed for cDNA libraries' generation.

snRNA-seq library preparation, sequencing, and raw data processing

Single-nuclei suspensions were loaded onto 10x Genomics Single Cell 3′ Chips (v 3.1) with the master mix according to the manufacturer's protocol (https://cdn.10xgenomics.com/image/upload/v1722285481/support-documents/CG000315_ChromiumNextGEMSingleCell3__GeneExpression_v3.1_DualIndex__RevF.pdf) for the Chromium Single Cell 3′ Library to generate single-nuclei gel beads in emulsion (GEMs, v3 chemistry). The libraries were sequenced on a NovaSeq 6000 using the following protocol: 28 cycles of Read1, 98 cycles of Read2, and 8 cycles of Index1 with a 200-cycle kit. Raw base calls were demultiplexed and converted to fastq files with the cellranger mkfastq program (bcl2fastq 2.20/cellranger 6.0) for subsequent processing and analysis.

Bioinformatic analysis

As this study focused on a dynamic reprogramming process where transcriptional changes are tightly associated with specific time points, we prioritized temporal resolution to capture the progression of cellular identity shifts over time. In addition, we performed unbiased clustering of the entire dataset comprising nuclei from both controls and multiple reprogramming time points.

The raw snRNA-seq data were mapped using 10X cellranger with the reference transcriptome GRCh38-2020-A. Scanpy (*83*) (version 1.9.3 with Python version 3.10.12) was used for the downstream analysis of the snRNA data. Cells with fewer than 1000 genes or more than 5% mitochondrial count were filtered out. Doublet detection and removal were performed using Scrublet. After filtering, the median UMI count was 3516, and the number of detected genes was 33512. Normalization and log transformation were performed, after which 3642 highly variable genes were identified. The Scanpy implementation of PCA dimensionality reduction was then used on the highly variable genes plus a selection of genes relevant to the desired conversion.

For UMAP projection and clustering, the 20 nearest neighbors were used, and the minimum distance was set to 0.05. For integration with the published dataset, eHarmonypy was used, converging after eight iterations. To further assess cell types, cosine similarities were calculated on the basis of the top 50 harmony-adjusted principal components, effectively comparing batch-corrected gene expression patterns (*79*). Similarly expressed genes for matching experimental and reference cell clusters were calculated by computing their mean gene expressions and their fold changes relative to the remaining integrated cells. The product of fold changes for each pair of matching reference and experimental cell cluster was then used to rank similarly expressed genes. We define the root of this value as their shared score. Genes expressed in less than 10% of cells in the matching clusters were omitted.

Differential gene expression analysis was done using the Wilcoxon rank sum test as implemented by Scanpy, and genes with a false discovery rate (FDR)–adjusted *P* value of <0.05 were considered significant. The Python package GSEApy (*84*) was used for GSEA on the top 100 differentially expressed genes for different clusters and time points, with the following databases: "GO Biological Process 2023," "GO Cellular Component 2023," and "GO Molecular Function 2023," as well as the corresponding database versions from 2021. For RNA velocity analysis, the Python package scVelo (*58*) was used. The velocity analysis was applied to a combined dataset of days 1 through 21 as the main gene expression changes were assumed to start happening at day 1, omitting day 0 to not dilute the

signal. Plots were produced with the Scanpy, scVelo, GSEApy, and Matplotlib Python packages.

Microscopy and PV quantification

Fluorescent images were taken with a Zeiss 780 Confocal Laser-Scanning Inverted Microscope (20X objective and 40X objective) and with Zeiss Zen Blue Edition software. For the 40X pictures, the HDR mode was used. Images were edited on ImageJ (NIH, Bethesda, MA, USA) and the changes were applied equally across the entire image without loss of information. Quantification of PV-expressing cells in spheroids was performed in ImageJ (NIH, Bethesda, MA, USA) by manually counting the individual PV+ cells in all the 1-µm-thick *z*-stacks of the confocal images. Bright-field images were captured with an Olympus IX50 Inverted Phase Contrast Microscope and acquired with CellSens Standard software.

High-content screening

The neuronal purity and PV yield in 2D were manually calculated as the number of TAU+ cells over the DAPI+ nuclei and PV+ cells over TAU+ cells, respectively, using the Operetta High Content Imaging System and the Harmony 5.2 software (Waltham, MA, USA). For each experiment, 371 to 379 fields (20X magnification) from one well were analyzed. The measurement of the mean fluorescence for antigen-positive cells was defined above the background fluorescence of antigen-negative cells (internal negative control). The same strategy was used for the analysis of the number of PV+ cells containing DAPI+ nuclei and expressing TAU. Using the "Neurite Outgrowth" script on Harmony 5.2 (PerkinElmer, USA), the total neurite length and segment length were quantified for PV+/TAU+ neurons. Quantifications of fig. S1C were performed similarly.

Statistical analysis

Statistical analyses were performed using GraphPad Prism 9.4.1. A Shapiro-Wilk normality test was applied to assess the normality of the distribution, and parametric and nonparametric tests were performed accordingly. PV+ cell quantifications, RT-qPCR, and electrophysiology data were compared using either one-way analysis of variance (ANOVA) followed by post hoc Tukey test or nonparametric Kruskal-Wallis test and uncorrected Dunn's test. RT-qPCR data, neurite analysis, and PV quantification in fig. S6 were compared using either an unpaired *t* test or the Mann-Whitney test. All data are expressed as means ± SEM. The level of statistical significance was set at $P < 0.05$.

Supplementary Materials

The PDF file includes:

Figs. S1 to S7
Tables S1 to S8
Legend for movie S1

Other Supplementary Material for this manuscript includes the following:

Movie S1

REFERENCES

1. R. Vignoles, C. Lentini, M. d'Orange, C. Heinrich, Direct lineage reprogramming for brain repair: Breakthroughs and challenges. *Trends Mol. Med.* **25**, 897–914 (2019).
2. R. A. Barker, M. Gotz, M. Parmar, New approaches for brain repair—From rescue to reprogramming. *Nature* **557**, 329–334 (2018).
3. M. Pereira, M. Birtele, D. R. Ottosson, Direct reprogramming into interneurons: Potential for brain repair. *Cell. Mol. Life Sci.* **76**, 3953–3967 (2019).
4. O. Torper, D. R. Ottosson, M. Pereira, S. Lau, T. Cardoso, S. Grealish, M. Parmar, In vivo reprogramming of striatal NG2 glia into functional neurons that integrate into local host circuitry. *Cell Rep.* **12**, 474–481 (2015).
5. C. Lentini, M. d'Orange, N. Marichal, M.-M. Trottmann, R. Vignoles, L. Foucault, C. Verrier, C. Massera, O. Raineteau, K.-K. Conzelmann, S. Rival-Gervier, A. Depaulis, B. Berninger, C. Heinrich, Reprogramming reactive glia into interneurons reduces chronic seizure activity in a mouse model of mesial temporal lobe epilepsy. *Cell Stem Cell* **28**, 2104–2121.e10 (2021).
6. Z. Y. Guo, L. Zhang, Z. Wu, Y. C. Chen, F. Wang, G. Chen, In vivo direct reprogramming of reactive glial cells into functional neurons after brain injury and in an Alzheimer's disease model. *Cell Stem Cell* **14**, 188–202 (2014).
7. J. Giehrl-Schwab, F. Giesert, B. Rauser, C. L. Lao, S. Hembach, S. Lefort, I. L. Ibarra, C. Koupourtidou, M. D. Luecken, D.-J. J. Truong, J. Fischer-Sternjak, G. Masserdotti, N. Prakash, J. Ninkovic, S. M. Hölter, D. M. V. Weisenhorn, F. J. Theis, M. Götz, W. Wurst, Parkinson's disease motor symptoms rescue by CRISPRa-reprogramming astrocytes into GABAergic neurons. *EMBO Mol. Med.* **14**, e14797 (2022).
8. N. Mattugini, R. Bocchi, V. Scheuss, G. L. Russo, O. Torper, C. L. Lao, M. Götz, Inducing different neuronal subtypes from astrocytes in the injured mouse cerebral cortex. *Neuron* **103**, 1086–1095.e5 (2019).
9. C. Heinrich, M. Bergami, S. Gascón, A. Lepier, F. Viganò, L. Dimou, B. Sutor, B. Berninger, M. Götz, Sox2-mediated conversion of NG2 glia into induced neurons in the injured adult cerebral cortex. *Stem Cell Rep.* **3**, 1000–1014 (2014).
10. C. Heinrich, S. Gascón, G. Masserdotti, A. Lepier, R. Sanchez, T. Simon-Ebert, T. Schroeder, M. Götz, B. Berninger, Generation of subtype-specific neurons from postnatal astroglia of the mouse cerebral cortex. *Nat. Protoc.* **6**, 214–228 (2011).
11. M. Pereira, M. Birtele, S. Shrigley, J. A. Benitez, E. Hedlund, M. Parmar, D. R. Ottosson, Direct reprogramming of resident NG2 glia into neurons with properties of fast-spiking parvalbumin-containing interneurons. *Stem Cell Rep.* **9**, 742–751 (2017).
12. M. Chouchane, A. R. M. de Farias, D. M. D. Moura, M. M. Hilscher, T. Schroeder, R. N. Leao, M. R. Costa, Lineage reprogramming of astroglial cells from different origins into distinct neuronal subtypes. *Stem Cell Rep.* **9**, 162–176 (2017).
13. N. Marichal, S. Peron, A. Beltran Arranz, C. Galante, F. Franco Scarante, R. Wiffen, C. Schuurmans, M. Karow, S. Gascon, B. Berninger, Reprogramming astroglia into neurons with hallmarks of fast-spiking parvalbumin-positive interneurons by phospho-site-deficient Ascl1. *Sci. Adv.* **10**, eadl5935 (2024).
14. J. M. Levine, R. Reynolds, J. W. Fawcett, The oligodendrocyte precursor cell in health and disease. *Trends Neurosci.* **24**, 39–47 (2001).
15. E. G. Hughes, S. H. Kang, M. Fukaya, D. E. Bergles, Oligodendrocyte progenitors balance growth with self-repulsion to achieve homeostasis in the adult brain. *Nat. Neurosci.* **16**, 668–676 (2013).
16. N. Kessaris, M. Fogarty, P. Iannarelli, M. Grist, M. Wegner, W. D. Richardson, Competing waves of oligodendrocytes in the forebrain and postnatal elimination of an embryonic lineage. *Nat. Neurosci.* **9**, 173–179 (2006).
17. E. van Tilborg, C. G. M. de Theije, M. van Hal, N. Wagenaar, L. S. de Vries, M. J. Benders, D. H. Rowitch, C. H. Nijboer, Origin and dynamics of oligodendrocytes in the developing brain: Implications for perinatal white matter injury. *Glia* **66**, 221–238 (2018).
18. S. Nolbrant, J. Giacomoni, D. B. Hoban, A. Bruzelius, M. Birtele, D. Chandler-Militello, M. Pereira, D. R. Ottosson, S. A. Goldman, M. Parmar, Direct reprogramming of human fetal- and stem cell-derived glial progenitor cells into midbrain dopaminergic neurons. *Stem Cell Rep.* **15**, 869–882 (2020).
19. S. Wang, J. Bates, X. Li, S. Schanz, D. Chandler-Militello, C. Levine, N. Maherali, L. Studer, K. Hochedlinger, M. Windrem, S. A. Goldman, Human iPSC-derived oligodendrocyte progenitor cells can myelinate and rescue a mouse model of congenital hypomyelination. *Cell Stem Cell* **12**, 252–264 (2013).
20. J. Giacomoni, A. Bruzelius, C. A. Stamouli, D. R. Ottosson, Direct conversion of human stem cell-derived glial progenitor cells into GABAergic interneurons. *Cells* **9**, 2451 (2020).
21. Y. Kubota, Untangling GABAergic wiring in the cortical microcircuit. *Curr. Opin. Neurobiol.* **26**, 7–14 (2014).
22. D. D. Rupert, S. D. Shea, Parvalbumin-positive interneurons regulate cortical sensory plasticity in adulthood and development through shared mechanisms. *Front. Neural Circuits* **16**, 886629 (2022).
23. S. Hijazi, A. B. Smit, R. E. van Kesteren, Fast-spiking parvalbumin-positive interneurons in brain physiology and Alzheimer's disease. *Mol. Psychiatry* **28**, 4954–4967 (2023).
24. L. E. Arroyo-García, A. G. Isla, Y. Andrade-Talavera, H. Balleza-Tapia, R. Loera-Valencia, L. Alvarez-Jimenez, G. Pizzirusso, S. Tambaro, P. Nilsson, A. Fisahn, Impaired spike-gamma coupling of area CA3 fast-spiking interneurons as the earliest functional impairment in the $App^{NL\text{-}G\text{-}F}$ mouse model of Alzheimer's disease. *Mol. Psychiatry* **26**, 5557–5567 (2021).
25. M. Martinez-Losa, T. E. Tracy, K. Ma, L. Verret, A. Clemente-Perez, A. S. Khan, I. Cobos, K. Ho, L. Gan, L. Mucke, M. Alvarez-Dolado, J. J. Palop, Nav1.1-overexpressing interneuron transplants restore brain rhythms and cognition in a mouse model of Alzheimer's disease. *Neuron* **98**, 75–89.e5 (2018).

26. O. Marín, Interneuron dysfunction in psychiatric disorders. *Nat. Rev. Neurosci.* **13**, 107–120 (2012).
27. D. G. Southwell, C. R. Nicholas, A. I. Basbaum, M. P. Stryker, A. R. Kriegstein, J. L. Rubenstein, A. Alvarez-Buylla, Interneurons from embryonic development to cell-based therapy. *Science* **344**, 1240622 (2014).
28. L. Verret, E. O. Mann, G. B. Hang, A. M. I. Barth, I. Cobos, K. Ho, N. Devidze, E. Masliah, A. C. Kreitzer, I. Mody, L. Mucke, J. J. Palop, Inhibitory interneuron deficit links altered network activity and cognitive dysfunction in Alzheimer model. *Cell* **149**, 708–721 (2012).
29. M. Bershteyn, S. Bröer, M. Parekh, Y. Maury, S. Havlicek, S. Kriks, L. Fuentealba, S. N. Lee, R. B. Zhou, G. Subramanyam, M. Sezan, E. S. Sevilla, W. Blankenberger, J. Spatazza, L. Zhou, H. Nethercott, D. Traver, P. Hampel, H. Kim, M. Watson, N. Salter, A. Nesterova, W. Au, A. Kriegstein, A. Alvarez-Buylla, J. Rubenstein, G. Banik, A. Bulfone, C. Priest, C. R. Nicholas, Human pallial MGE-type GABAergic interneuron cell therapy for chronic focal epilepsy. *Cell Stem Cell* **30**, 1331–1350.e11 (2023).
30. C. R. Nicholas, J. D. Chen, Y. S. Tang, D. G. Southwell, N. Chalmers, D. Vogt, C. M. Arnold, Y. J. J. Chen, E. G. Stanley, A. G. Elefanty, Y. Sasai, A. Alvarez-Buylla, J. L. R. Rubenstein, A. R. Kriegstein, Functional maturation of hPSC-derived forebrain interneurons requires an extended timeline and mimics human neural development. *Cell Stem Cell* **12**, 573–586 (2013).
31. A. M. Maroof, S. Keros, J. A. Tyson, S. W. Ying, Y. M. Ganat, F. T. Merkle, B. Liu, A. Goulburn, E. G. Stanley, A. G. Elefanty, H. R. Widmer, K. Eggan, P. A. Goldstein, S. A. Anderson, L. Studer, Directed differentiation and functional maturation of cortical interneurons from human embryonic stem cells. *Cell Stem Cell* **12**, 559–572 (2013).
32. M. C. Varela, M. P. Walker, J. Bok, E. L. Crespo, T. Thenstedt, L. Goldstein, A. M. Tidball, J. Z. Li, Y. Yuan, L. L. Isom, J. Fu, M. Uhler, J. M. Parent, Robust Production of Parvalbumin Interneurons and Fast-Spiking Neurons from Human Medial Ganglionic Eminence Organoids. bioRxiv 662594 [Preprint] (2025). https://doi.org/10.1101/2025.07.01.662594.
33. R. M. Walsh, G. W. Crabtree, K. Kalpana, L. Jubierre, S. Y. Koo, G. Ciceri, J. A. Gogos, I. Kruglikov, L. Studer, Forebrain assembloids support the development of fast-spiking human PVALB+ cortical interneurons and uncover schizophrenia-associated defects. *Neuron* **113**, 3185–3203.e7 (2025).
34. G. Colasante, G. Lignani, A. Rubio, L. Medrihan, L. Yekhlef, A. Sessa, L. Massimino, S. G. Giannelli, S. Sacchetti, M. Caiazzo, D. Leo, D. Alexopoulou, M. T. Dell'Anno, E. Ciabatti, M. Orlando, M. Studer, A. Dahl, R. R. Gainetdinov, S. Taverna, F. Benfenati, V. Broccoli, Rapid conversion of fibroblasts into functional forebrain GABAergic interneurons by direct genetic reprogramming. *Cell Stem Cell* **17**, 719–734 (2015).
35. W. Huang, A. Bhaduri, D. Velmeshev, S. Wang, L. Wang, C. A. Rottkamp, A. Alvarez-Buylla, D. H. Rowitch, A. R. Kriegstein, Origins and proliferative states of human oligodendrocyte precursor cells. *Cell* **182**, 594–608.e11 (2020).
36. M. P. Serrano-Regal, I. Luengas-Escuza, L. Bayon-Cordero, N. Ibarra-Aizpurua, E. Alberdi, A. Perez-Samartin, C. Matute, M. V. Sanchez-Gomez, Oligodendrocyte differentiation and myelination is potentiated via $GABA_B$ receptor activation. *Neuroscience* **439**, 163–180 (2020).
37. J. Giacomoni, A. Bruzelius, M. Habekost, J. Kajtez, D. R. Ottosson, A. Fiorenzano, P. Storm, M. Parmar, 3D model for human glia conversion into subtype-specific neurons, including dopamine neurons. *Cell Rep. Methods* **4**, 100845 (2024).
38. L. Wang, C. Wang, J. A. Moriano, S. Chen, G. Zuo, A. Cebrian-Silla, S. Zhang, T. Mukhtar, S. Wang, M. Song, L. G. de Oliveira, Q. Bi, J. J. Augustin, X. Ge, M. F. Paredes, E. J. Huang, A. Alvarez-Buylla, X. Duan, J. Li, A. R. Kriegstein, Molecular and cellular dynamics of the developing human neocortex. *Nature* **647**, 169–178 (2025).
39. D. van Bruggen, F. Pohl, C. M. Langseth, P. Kukanja, H. Lee, A. M. Albiach, M. Kabbe, M. Meijer, S. Linnarsson, M. M. Hilscher, M. Nilsson, E. Sundstrom, G. Castelo-Branco, Developmental landscape of human forebrain at a single-cell level identifies early waves of oligodendrogenesis. *Dev. Cell* **57**, 1421–1436.e5 (2022).
40. D. Velmeshev, Y. Perez, Z. Yan, J. E. Valencia, D. R. Castaneda-Castellanos, L. Wang, L. Schirmer, S. Mayer, B. Wick, S. Wang, T. J. Nowakowski, M. Paredes, E. J. Huang, A. R. Kriegstein, Single-cell analysis of prenatal and postnatal human cortical development. *Science* **382**, eadf0834 (2023).
41. J. J. Boulanger, C. Messier, Doublecortin in oligodendrocyte precursor cells in the adult mouse brain. *Front. Neurosci.* **11**, 143 (2017).
42. H. Hu, P. Jonas, A supercritical density of Na^+ channels ensures fast signaling in GABAergic interneuron axons. *Nat. Neurosci.* **17**, 686–693 (2014).
43. W. H. Cuddleston, J. Li, X. Fan, A. Kozenkov, M. Lalli, S. Khalique, S. Dracheva, E. A. Mukamel, M. S. Breen, Cellular and genetic drivers of RNA editing variation in the human brain. *Nat. Commun.* **13**, 2997 (2022).
44. B. R. E. Ansell, S. N. Thomas, R. Bonelli, J. E. Munro, S. Freytag, M. Bahlo, A survey of RNA editing at single-cell resolution links interneurons to schizophrenia and autism. *RNA* **27**, 1482–1496 (2021).
45. A. Paul, M. Crow, R. Raudales, M. He, J. Gillis, Z. J. Huang, Transcriptional architecture of synaptic communication delineates GABAergic neuron identity. *Cell* **171**, 522–539.e20 (2017).
46. J. Arikkath, I. Israely, Y. Tao, L. Mei, X. Liu, L. F. Reichardt, Erbin controls dendritic morphogenesis by regulating localization of delta-catenin. *J. Neurosci.* **28**, 7047–7056 (2008).
47. J. B. Manneville, M. Jehanno, S. Etienne-Manneville, Dlg1 binds GKAP to control dynein association with microtubules, centrosome positioning, and cell polarity. *J. Cell Biol.* **191**, 585–598 (2010).
48. E. Hong, P. Jayachandran, R. Brewster, The polarity protein Pard3 is required for centrosome positioning during neurulation. *Dev. Biol.* **341**, 335–345 (2010).
49. D. P. Meka, R. Scharrenberg, F. Calderon de Anda, Emerging roles of the centrosome in neuronal development. *Cytoskeleton* **77**, 84–96 (2020).
50. D. Carulli, F. de Winter, J. Verhaagen, Semaphorins in adult nervous system plasticity and disease. *Front. Synaptic Neurosci.* **13**, 672891 (2021).
51. A. Steinecke, C. Gampe, G. Zimmer, J. Rudolph, J. Bolz, EphA/ephrin A reverse signaling promotes the migration of cortical interneurons from the medial ganglionic eminence. *Development* **141**, 460–471 (2014).
52. A. V. Zaitsev, N. V. Povysheva, D. A. Lewis, L. S. Krimer, P/Q-type, but not N-type, calcium channels mediate GABA release from fast-spiking interneurons to pyramidal cells in rat prefrontal cortex. *J. Neurophysiol.* **97**, 3567–3573 (2007).
53. P. Juarez, V. M. Cerdeño, Parvalbumin and parvalbumin chandelier interneurons in autism and other psychiatric disorders. *Front. Psych.* **13**, 913550 (2022).
54. B. Tasic, Z. Yao, L. T. Graybuck, K. A. Smith, T. N. Nguyen, D. Bertagnolli, J. Goldy, E. Garren, M. N. Economo, S. Viswanathan, O. Penn, T. Bakken, V. Menon, J. Miller, O. Fong, K. E. Hirokawa, K. Lathia, C. Rimorin, M. Tieu, R. Larsen, T. Casper, E. Barkan, M. Kroll, S. Parry, N. V. Shapovalova, D. Hirschstein, J. Pendergraft, H. A. Sullivan, T. K. Kim, A. Szafer, N. Dee, P. Groblewski, I. Wickersham, A. Cetin, J. A. Harris, B. P. Levi, S. M. Sunkin, L. Madisen, T. L. Daigle, L. Looger, A. Bernard, J. Phillips, E. Lein, M. Hawrylycz, K. Svoboda, A. R. Jones, C. Koch, H. Zeng, Shared and distinct transcriptomic cell types across neocortical areas. *Nature* **563**, 72–78 (2018).
55. R. D. Hodge, T. E. Bakken, J. A. Miller, K. A. Smith, E. R. Barkan, L. T. Graybuck, J. L. Close, B. Long, N. Johansen, O. Penn, Z. Z. Yao, J. Eggermont, T. Höllt, B. P. Levi, S. I. Shehata, B. Aevermann, A. Beller, D. Bertagnolli, K. Brouner, T. Casper, C. Cobbs, R. Dalley, N. Dee, S. L. Ding, R. G. Ellenbogen, O. Fong, E. Garren, J. Goldy, R. P. Gwinn, D. Hirschstein, C. D. Keene, M. Keshk, A. L. Ko, K. Lathia, A. Mahfouz, Z. Maltzer, M. McGraw, T. N. Nguyen, J. Nyhus, J. G. Ojemann, A. Oldre, S. Parry, S. Reynolds, C. Rimorin, N. V. Shapovalova, S. Somasundaram, A. Szafer, E. R. Thomsen, M. Tieu, G. Quon, R. H. Scheuermann, R. Yuste, S. M. Sunkin, B. Lelieveldt, D. Feng, L. Ng, A. Bernard, M. Hawrylycz, J. W. Phillips, B. Tasic, H. K. Zeng, A. R. Jones, C. Koch, E. S. Lein, Conserved cell types with divergent features in human versus mouse cortex. *Nature* **573**, 61–68 (2019).
56. T. E. Bakken, N. L. Jorstad, Q. Hu, B. B. Lake, W. Tian, B. E. Kalmbach, M. Crow, R. D. Hodge, F. M. Krienen, S. A. Sorensen, J. Eggermont, Z. Yao, B. D. Aevermann, A. I. Aldridge, A. Bartlett, D. Bertagnolli, T. Casper, R. G. Castanon, K. Crichton, T. L. Daigle, R. Dalley, N. Dee, N. Dembrow, D. Diep, S.-L. Ding, W. Dong, R. Fang, S. Fischer, M. Goldman, J. Goldy, L. T. Graybuck, B. R. Herb, X. Hou, J. Kancherla, M. Kroll, K. Lathia, B. van Lew, Y. E. Li, C. S. Liu, H. Liu, J. D. Lucero, A. Mahurkar, D. M. Millen, J. A. Miller, M. Moussa, J. R. Nery, P. R. Nicovich, S.-Y. Niu, J. Orvis, J. K. Osteen, S. Owen, C. R. Palmer, T. Pham, N. Plongthongkum, O. Poirion, N. M. Reed, C. Rimorin, A. Rivkin, W. J. Romanow, A. E. Sedeño-Cortés, K. Siletti, S. Somasundaram, J. Sulc, M. Tieu, A. Torkelson, H. Tung, X. Wang, F. Xie, A. M. Yanny, R. Zhang, S. A. Ament, M. M. Behrens, H. C. Bravo, J. Chun, A. Dobin, J. Gillis, R. Hertzano, P. R. Hof, T. Höllt, G. D. Horwitz, C. D. Keene, P. V. Kharchenko, A. L. Ko, B. P. Lelieveldt, C. Luo, E. A. Mukamel, A. Pinto-Duarte, S. Preissl, A. Regev, B. Ren, R. H. Scheuermann, K. Smith, W. J. Spain, O. R. White, C. Koch, M. Hawrylycz, B. Tasic, E. Z. Macosko, S. A. McCarroll, J. T. Ting, H. Zeng, K. Zhang, G. Feng, J. R. Ecker, S. Linnarsson, E. S. Lein, Comparative cellular analysis of motor cortex in human, marmoset and mouse. *Nature* **598**, 111–119 (2021).
57. E. Favuzzi, R. Deogracias, A. Marques-Smith, P. Maeso, J. Jezequel, D. Exposito-Alonso, M. Balia, T. Kroon, A. J. Hinojosa, E. F. Maraver, B. Rico, Distinct molecular programs regulate synapse specificity in cortical inhibitory circuits. *Science* **363**, 413–417 (2019).
58. V. Bergen, M. Lange, S. Peidli, F. A. Wolf, F. J. Theis, Generalizing RNA velocity to transient cell states through dynamical modeling. *Nat. Biotechnol.* **38**, 1408–1414 (2020).
59. F. A. Wolf, F. K. Hamey, M. Plass, J. Solana, J. S. Dahlin, B. Göttgens, N. Rajewsky, L. Simon, F. J. Theis, PAGA: Graph abstraction reconciles clustering with trajectory inference through a topology preserving map of single cells. *Genome Biol.* **20**, 59 (2019).
60. L. A. B. Elias, G. B. Potter, A. R. Kriegstein, A time and a place for Nkx2-1 in interneuron specification and migration. *Neuron* **59**, 679–682 (2008).
61. O. Marin, Parvalbumin interneuron deficits in schizophrenia. *Eur. Neuropsychopharmacol.* **82**, 44–52 (2024).
62. L. Zhang, Z. H. Qin, K. M. Ricke, S. A. Cruz, A. F. R. Stewart, H. H. Chen, Hyperactivated PTP1B phosphatase in parvalbumin neurons alters anterior cingulate inhibitory circuits and induces autism-like behaviors. *Nat. Commun.* **11**, 44–52 (2020).
63. N. Dehorter, N. Marichal, O. Marín, B. Berninger, Tuning neural circuits by turning the interneuron knob. *Curr. Opin. Neurobiol.* **42**, 144–151 (2017).

64. L. Dimou, M. Gotz, Glial cells as progenitors and stem cells: New roles in the healthy and diseased brain. *Physiol. Rev.* **94**, 709–737 (2014).
65. T. Allison, J. Langerman, S. Sabri, M. Otero-Garcia, A. Lund, J. Huang, X. Wei, R. A. Samarasinghe, D. Polioudakis, I. Mody, I. Cobos, B. G. Novitch, D. H. Geschwind, K. Plath, W. E. Lowry, Defining the nature of human pluripotent stem cell-derived interneurons via single-cell analysis. *Stem Cell Rep.* **16**, 2548–2564 (2021).
66. J. L. Close, Z. Z. Yao, B. P. Levi, J. A. Miller, T. E. Bakken, V. Menon, J. T. Ting, A. Wall, A. R. Krostag, E. R. Thomsen, A. M. Nelson, J. K. Mich, R. D. Hodge, S. I. Shehata, I. A. Glass, S. Bort, N. V. Shapovalova, N. K. Ngo, J. S. Grimley, J. W. Phillips, C. L. Thompson, S. Ramanathan, E. Lein, Single-cell profiling of an in vitro model of human interneuron development reveals temporal dynamics of cell type production and maturation. *Neuron* **96**, 949–949 (2017).
67. M. Karow, J. G. Camp, S. Falk, T. Gerber, A. Pataskar, M. Gac-Santel, J. Kageyama, A. Brazovskaja, A. Garding, W. Fan, T. Riedemann, A. Casamassa, A. Smiyakin, C. Schichor, M. Gotz, V. K. Tiwari, B. Treutlein, B. Berninger, Direct pericyte-to-neuron reprogramming via unfolding of a neural stem cell-like program. *Nat. Neurosci.* **21**, 932–940 (2018).
68. K. Katayama, F. Imai, K. Campbell, R. A. Lang, Y. Zheng, Y. Yoshida, RhoA and Cdc42 are required in pre-migratory progenitors of the medial ganglionic eminence ventricular zone for proper cortical interneuron migration. *Development* **140**, 3139–3145 (2013).
69. A. C. O'Neill, C. Kyrousi, J. Klaus, R. J. Leventer, E. P. Kirk, A. Fry, D. T. Pilz, T. Morgan, Z. A. Jenkins, M. Drukker, S. F. Berkovic, I. E. Scheffer, R. Guerrini, D. M. Markie, M. Götz, S. Cappello, S. P. Robertson, A primate-specific isoform of regulates neurogenesis and neuronal migration. *Cell Rep.* **25**, 2729–2741.e6 (2018).
70. N. R. Reinhard, S. Van Der Niet, A. Chertkova, M. Postma, P. L. Hordijk, T. W. J. Gadella Jr., J. Goedhart, Identification of guanine nucleotide exchange factors that increase Cdc42 activity in primary human endothelial cells. *Small GTPases* **12**, 226–240 (2021).
71. C. M. Aldaz, T. Hussain, WWOX loss of function in neurodevelopmental and neurodegenerative disorders. *Int. J. Mol. Sci.* **21**, 8922 (2020).
72. T. Hussain, H. Kil, B. Hattiangady, J. Lee, M. Kodali, B. Shuai, S. Attaluri, Y. Takata, J. J. Shen, M. C. Abba, A. K. Shetty, C. M. Aldaz, *Wwox* deletion leads to reduced GABA-ergic inhibitory interneuron numbers and activation of microglia and astrocytes in mouse hippocampus. *Neurobiol. Dis.* **121**, 163–176 (2019).
73. M. Iacomino, S. Baldassari, Y. Tochigi, K. Kośla, F. Buffelli, A. Torella, M. Severino, D. Paladini, L. Mandarà, A. Riva, M. Scala, G. Balagura, A. Accogli, V. Nigro, C. Minetti, E. Fulcheri, F. Zara, A. K. Bednarek, P. Striano, H. Suzuki, V. Salpietro, The WWOX gene depletion impairs neural cell migration process and may disrupt brain development. *Front. Neurosci.* **9**, 206–206 (2019).
74. N. B. Gallo, A. Paul, L. Van Aelst, Shedding light on chandelier cell development, connectivity, and contribution to neural disorders. *Trends Neurosci.* **43**, 565–580 (2020).
75. T. C. Südhof, Synaptic neurexin complexes: A molecular code for the logic of neural circuits. *Cell* **171**, 745–769 (2017).
76. E. K. Lucas, S. E. Dougherty, L. J. McMeekin, C. S. Reid, L. E. Dobrunz, A. B. West, J. J. Hablitz, R. M. Cowell, PGC-1α provides a transcriptional framework for synchronous neurotransmitter release from parvalbumin-positive interneurons. *J. Neurosci.* **34**, 14375–14387 (2014).
77. S. Gascón, E. Murenu, G. Masserdotti, F. Ortega, G. L. Russo, D. Petrik, A. Deshpande, C. Heinrich, M. Karow, S. P. Robertson, T. Schroeder, J. Beckers, M. Irmler, C. Berndt, J. P. F. Angeli, M. Conrad, B. Berninger, M. Götz, Identification and successful negotiation of a metabolic checkpoint in direct neuronal reprogramming. *Cell Stem Cell* **18**, 396–409 (2016).
78. H. Hu, J. Gan, P. Jonas, Fast-spiking, parvalbumin$^+$ GABAergic interneurons: From cellular design to microcircuit function. *Science* **345**, 1255263 (2014).
79. B. Georgievska, J. Jakobsson, E. Persson, C. Ericson, D. Kirik, C. Lundberg, Regulated delivery of glial cell line-derived neurotrophic factor into rat striatum, using a tetracycline-dependent lentiviral vector. *Hum. Gene Ther.* **15**, 934–944 (2004).
80. J. Giacomoni, M. Habekost, E. Cepeda-Prado, B. Mattsson, D. R. Ottosson, M. Parmar, J. Kajtez, Protocol for optical clearing and imaging of fluorescently labeled rat brain slices. *Star Protoc.* **4**, 102041 (2023).
81. N. Gvazava, S. C. Konings, E. Cepeda-Prado, V. Skoryk, C. H. Umeano, J. Dong, I. A. N. Silva, D. R. Ottosson, N. D. Leigh, D. E. Wagner, O. Klementieva, Label-free high-resolution photothermal optical infrared spectroscopy for spatiotemporal chemical analysis in fresh, hydrated living tissues and embryos. *J. Am. Chem. Soc.* **145**, 24796–24808 (2023).
82. E. Sodersten, K. Toskas, V. Rraklli, K. Tiklova, A. K. Bjorklund, M. Ringner, T. Perlmann, J. Holmberg, A comprehensive map coupling histone modifications with gene regulation in adult dopaminergic and serotonergic neurons. *Nat. Commun.* **9**, 1226 (2018).
83. F. A. Wolf, P. Angerer, F. J. Theis, SCANPY: Large-scale single-cell gene expression data analysis. *Genome Biol.* **19**, 15 (2018).
84. Z. Fang, X. Liu, G. Peltz, GSEApy: A comprehensive package for performing gene set enrichment analysis in Python. *Bioinformatics* **39**, btac757 (2023).

Acknowledgments: This work was supported by several core facilities funded by the Lund Stem Cell Center and MultiPark. We would like to thank A. Hammarberg for assistance with nuclei sorting, J. Johansson for cDNA library preparation, E. Monni for assistance with confocal imaging, and P. Storm for valuable suggestions and discussion. This work was also supported by the Knut and Alice Wallenberg Foundation (KAW 2021-0088) to SciLifeLab for research in Data-driven Life Science, DDLS (KAW 2020.0239), and partially supported by the Wallenberg AI, Autonomous Systems and Software Program (WASP) funded by the Knut and Alice Wallenberg Foundation. **Funding:** This work was supported by the Swedish Research Council 2021-01839 and 2021-03149 (D.R.O.); Knut and Alice Wallenberg Foundation 2021-0088 (D.R.O.); Crafoord Foundation 20231012 (D.R.O.); Jeansson Foundation JS2018-0103; Brain Foundation FO2019-0195 (D.R.O.); Åhléns Foundation 139208 (D.R.O.); Royal Physiographical Society and Per-Eric Ulla Schyberg Foundation, Sweden (E.C.-P. and D.R.O.); Olle Engkvist Foundation 213-0229 (D.R.O.); Anna-Lisa Rosenberg Foundation and Royal Physiographic Society in Lund 43202 (D.R.O.); and NanoLund, grant p14-2023 (O.K.). **Author contributions:** Conceptualization: D.R.O., C.A.S., E.C.-P., J.G., O.K., M.P., and V.O. Methodology: C.A.S., A.D., E.C.-P., O.K., M.P., V.O., and D.R.O. Resources: D.R.O., J.G., V.O., M.P., and O.K. Investigation: C.A.S., A.D., E.C.-P., A.B., J.G., A.D.V., O.K., and D.R.O. Data curation: A.D., A.B., E.A., O.K., and V.O. Formal analysis: C.A.S., A.D., E.C.-P., A.B., J.G., E.A., A.D.V., O.K., and V.O. Software: A.D. and E.A. Validation: C.A.S., A.D., E.C.-P., A.B., O.K., V.O., and D.R.O. Visualization: C.A.S., A.D., E.C.-P., J.G., S.K., O.K., V.O., and D.R.O. Supervision: D.R.O., V.O., and M.P. Funding acquisition: D.R.O., O.K., M.P., and V.O. Project administration: D.R.O., M.P., and V.O. Writing—original draft: C.A.S., D.R.O., A.D., J.G., O.K., and V.O. Writing—review and editing: D.R.O., C.A.S., A.D., E.C.-P., A.B., J.G., S.K., A.D.V., O.K., M.P., and V.O. **Competing interests:** M.P. is the owner of Parmar Cells AB and a coinventor on US patent 15/093,927; EP17181588; PCT/EP2018/062261. Parmar Cells AB holds royalty agreements on patents related to cell reprogramming and stem cell–derived dopamine cell products. M.P. has academic research collaborations with Novo Nordisk A/S and Miltenyi Biotec, is a paid consultant for Novo Nordisk A/S, and serves as Scientific Advisory Board member of Arbor Bio. The other authors declare that they have no competing interests. **Data and materials availability:** All data and code needed to evaluate and reproduce the results in the paper are present in the paper and/or the Supplementary Materials. Processed RNA sequencing data and code can be found in: https://figshare.com/s/a377513962c7364b4686.

Submitted 6 December 2024
Accepted 25 November 2025
Published 1 January 2026
10.1126/sciadv.adv0588

ScienceAdvances

A distinct lineage pathway drives parvalbumin chandelier cell fate in human interneuron reprogramming

Christina A. Stamouli, Alexander Degener, Efrain Cepeda-Prado, Andreas Bruzelius, Emil Andersson, Jessica Giacomoni, Aurélie Delphine Vorgeat, Srisaiyini Kidnapillai, Oxana Klementieva, Malin Parmar, Victor Olariu, and Daniella Rylander Ottosson

Sci. Adv. **12** (1), eadv0588. DOI: 10.1126/sciadv.adv0588